

*M. Kriening, Z. Yao, M. S. Emran, J. Song, A. Teimurazov and O. Shishkina*

# On multiple stable states in Taylor–Couette flow with realistic end-wall boundary conditions

**Marvin Kriening, Zhongzhi Yao, Mohammad S. Emran, Jiaxing Song, Andrei Teimurazov and Olga Shishkina**

Max Planck Institute for Dynamics and Self-Organization, 37077 Göttingen, Germany

---

We investigate Taylor–Couette flow with realistic no-slip boundary conditions at all surfaces through direct numerical simulations (DNS) and theoretical analysis. Imposing physically consistent end-wall conditions at the top and bottom lids significantly alters the flow dynamics compared to that for periodic boundary conditions. We extend the classical angular-momentum-flux framework to account for axial transport, which leads to a significantly improved agreement with the Eckhardt–Grossmann–Lohse model (Eckhardt *et al.* 2007).

A systematic exploration of the parameter space ( $Re, n$ ) uncovers multiple long-lived states with different roll number  $n$  configurations at identical Reynolds numbers  $Re$ , giving rise to pronounced hysteresis loops occurring under realistic boundary conditions. Our DNS for no-slip axial end caps reveal a sequence of structural transitions: as the inner-cylinder Reynolds number increases, the flow evolves from Taylor vortex flow through chaotic wavy vortex flow and turbulent wavy vortex flow to an axisymmetric turbulent Taylor vortex flow. Using modal energy budgets we identify transition mechanisms and quantify how the accessible phase-space volume and associated roll-specific angular momentum flux depend on control parameters and the specific flow state.

Our findings demonstrate the impact of realistic boundary conditions on the dynamics in Taylor–Couette flow, and how they change the stability landscape of multiple states. The coexistence of distinct flow patterns and their stability analysis offers promising insights into transition dynamics between laminar and turbulent regimes in closed sheared flows.

## **1. Introduction**

Taylor–Couette (TC) flow, the motion of a fluid confined between two independently rotating concentric vertical cylinders, has served for over a century as a canonical model for understanding flow instabilities and turbulent dynamics in fluid mechanics. Its origins trace back to the pioneering experiments of Couette (1890), who first used the configuration as a viscometer, and Mallock (1896), who discovered early signs of turbulence when rotating the inner cylinder. Taylor’s seminal work (Taylor 1923) revealed the system’s linear instability, sparking a long tradition of experimental and theoretical investigation into the transition from laminar to turbulent flow. Subsequent studies by Wendt (1933) and Coles (1965), and many others have established TC flow as a benchmark for exploring fundamental questions in hydrodynamic stability, turbulence, and transport processes.

Despite its geometric simplicity, TC flow exhibits a remarkable variety of flow states. As the rotation rate of the inner cylinder increases, the base Couette flow gives way to axisymmetric, axially periodic, and temporally stationary Taylor vortices. Further increases in the driving parameters trigger a sequence of symmetry-breaking transitions. Patterns become increasingly intricate, evolving into wavy vortices, modulated structures, and eventually fully developed turbulence. Intriguingly, even in the turbulent regime, large-scale coherent structures persist, reflecting an interplay between order and disorder (Huisman *et al.* 2014).

When both cylinders rotate, particularly in the opposite directions, the range of accessible flow states expands dramatically, revealing multiple “routes” to turbulence. This progressive complexity makes TC flow not only a fertile testing ground for stability theory and turbulence modeling but also a bridge between fundamental physics and industrial applications (Schrumpf *et al.* 2021; Rudelstorfer *et al.* 2023).

Recent advancements in computational fluid dynamics have enabled high-fidelity simulations of TC flow, allowing for detailed investigation of turbulent structures and transport phenomena under various boundary conditions. Several studies (Coughlin & Marcus 1996; Batten *et al.* 2002; Bilson & Bremhorst 2007; Pirrò & Quadrio 2008; Brauckmann & Eckhardt 2013; Ostilla *et al.* 2013; Ostilla-Mónico *et al.* 2014) simulated turbulent TC flow for relatively high Taylor numbers up to  $Ta = 4.6 \times 10^{10}$ . Most of these simulations (Brauckmann & Eckhardt 2013; Ostilla *et al.* 2013; Ostilla-Mónico *et al.* 2014) employed periodic boundary conditions in the axial direction. However, imposing no-slip boundary conditions at the horizontal surfaces is crucial for accurately capturing the flow dynamics near the walls, where viscous effects are pronounced (Jeganathan *et al.* 2021). Differences between periodic and no-slip end-wall boundary conditions manifest not only in the formation of self-organized structures but also in the accessible phase space of temporarily stationary states. Realistic boundary conditions enable the system to reach highly asymmetric roll configurations. These states not only remain stable but also exhibit significantly higher angular momentum flux compared to symmetric states – a finding that, beyond its fundamental interest for system understanding, highlights substantial potential for engineering applications (Mamun & Tuckerman 1995; Xu *et al.* 2023).

Wall-bounded turbulent flows can exhibit different statistically stationary states even when control parameters remain identical (Ostilla-Mónico *et al.* 2014; Martínez-Arias *et al.* 2014; Ramesh *et al.* 2019). However, this phenomenon is not unique to Taylor–Couette flow – it has also been observed in other convective systems such as Rayleigh–Bénard convection (Ahlers *et al.* 2009; van der Poel *et al.* 2011; Wang *et al.* 2020), tilted convection (Wang *et al.* 2018), double diffusive convection (Yang *et al.* 2020) and magnetoconvection (McCormack *et al.* 2025) to name a few. Despite being known for several decades, this topic requires further investigation, as we are still far from a complete

understanding despite its profound significance for numerous fields where wall-bounded turbulence plays a central role.

In this study, we perform direct numerical simulations (DNS) of realistic TC flow for no-slip boundary conditions at all surfaces, with the outer cylinder fixed and the rotation rate of the inner cylinder systematically varied. A  $Re$  range of  $90 \leq Re \leq 7500$  is covered by mainly focusing on system geometries, which are characterized by  $\Gamma = 11$  and  $\Gamma = 30$ , respectively. The latter geometry has been chosen as our main investigation setup due to the broad spectrum for comparison with experimental data by Martínez-Arias *et al.* (2014), which covers a wide  $Re$  range characterized by several different flow states. We hence study multiple stable states in this geometry by systematically varying the inner Reynolds number  $Re_i$ .

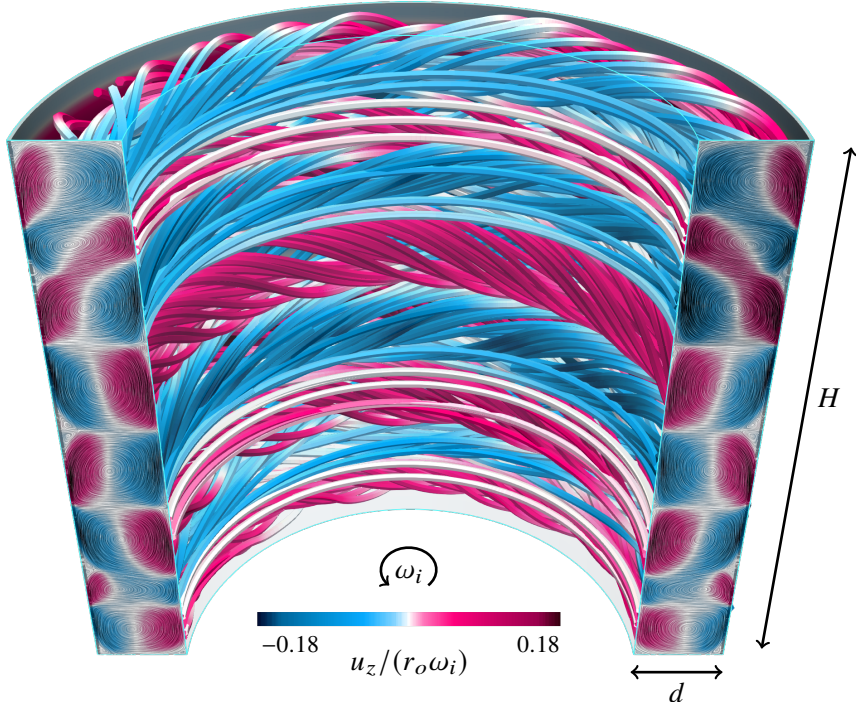


Figure 1. Example of a TC flow as obtained in the DNS for  $Re = 5600$ ,  $\Gamma = 2\pi$ ,  $\eta = 5/7$  as in the setup of Ostilla *et al.* (2013), but with solid top and bottom lids, illustrated by isosurfaces of the axial velocity  $u_z$ . Only half of the computational domain is shown.

The paper is organized as follows. Section 2 describes the Taylor–Couette system, governing equations, control and response parameters. Section 3 details our numerical implementation, including the treatment of wall-lid singularities and validates our numerical approach against experimental data. Sections 4 and 5 present the DNS results. Section 4 highlights changes in the global and local dynamics due to the realistic boundary conditions, while section 5 presents multiple stable states and hysteresis phenomena and discusses the underlying physical mechanisms. Section 6 concludes with a summary of our findings and future challenges.

## 2. System Description

### 2.1. Control parameters and governing equations

We consider the flow of an incompressible Newtonian fluid with kinematic viscosity  $\nu$  confined between two concentric vertical cylinders of radii  $r_i$  (inner) and  $r_o$  (outer) with height  $H$ . The inner cylinder rotates with angular frequency  $\omega_i$  while the outer cylinder remains stationary ( $\omega_o = 0$ ). Upper and lower plates rotate with the outer sidewall at the same angular frequency and therefore remain at rest within our system of consideration. The system is characterized by three dimensionless parameters: the radius ratio  $\eta$ , the aspect ratio  $\Gamma$ , and the Reynolds number  $Re$ ,

$$\eta = \frac{r_i}{r_o}, \quad \Gamma = \frac{H}{d}, \quad Re \equiv Re_i = \frac{\omega_i r_i d}{\nu}, \quad (2.1)$$

where  $d = r_o - r_i$  is the gap width. Another useful quantity we use is the Taylor number  $Ta$  (Eckhardt *et al.* 2007)

$$Ta \equiv \left( \frac{r_o + r_i}{2} \right)^6 \frac{d^2}{r_o^2 r_i^2 \nu^2} (\omega_o - \omega_i)^2. \quad (2.2)$$

The Navier–Stokes equations for incompressible TC flow in a rotating frame read:

$$\nabla \cdot \mathbf{u} = 0, \quad \frac{\partial \mathbf{u}}{\partial t} + (\mathbf{u} \cdot \nabla) \mathbf{u} = -\frac{1}{\rho} \nabla p + \nu \nabla^2 \mathbf{u} - 2\mathbf{Q} \times \mathbf{u}, \quad (2.3)$$

where  $\mathbf{u}$  is the velocity field,  $p$  is the pressure,  $\rho$  is the density,  $\nu$  is the kinematic viscosity,  $\mathbf{Q} = \omega_o \mathbf{e}_z$  with  $\omega_o$  the reference angular frequency, and  $\mathbf{e}_z$  the unit vector in the axial direction.

An example of an analyzed setup is shown in figure 1, which presents a cross-section of our Taylor–Couette system along with the axial flow field obtained from our DNS.

In cylindrical coordinates  $(r, \phi, z)$ , and under the assumption of a non-moving outer cylinder, they take the following form:

$$\partial_t u_r + (\mathbf{u} \cdot \nabla) u_r - \frac{u_\phi^2}{r} = -\frac{\partial_r p}{\rho} + \nu \left( \nabla^2 u_r - \frac{u_r}{r^2} - \frac{2}{r^2} \partial_\phi u_\phi \right), \quad (2.4)$$

$$\partial_t u_\phi + (\mathbf{u} \cdot \nabla) u_\phi + \frac{u_\phi u_r}{r} = -\frac{1}{r\rho} \partial_\phi p + \nu \left( \nabla^2 u_\phi - \frac{u_\phi}{r^2} + \frac{2}{r^2} \partial_\phi u_r \right), \quad (2.5)$$

$$\partial_t u_z + (\mathbf{u} \cdot \nabla) u_z = -\frac{\partial_z p}{\rho} + \nu \nabla^2 u_z, \quad (2.6)$$

$$0 = \frac{1}{r} \partial_r (r u_r) + \frac{1}{r} \partial_\phi u_\phi + \partial_z u_z, \quad (2.7)$$

where  $\mathbf{u} \equiv (u_r, u_\phi, u_z)$ . We impose no-slip conditions at all boundaries:

$$\begin{aligned} \text{Inner cylinder:} \quad & u_r = 0, \quad u_\phi = \psi r_i \omega_i, \quad u_z = 0 \quad \text{at } r = r_i \\ \text{Outer cylinder:} \quad & u_r = 0, \quad u_\phi = 0, \quad u_z = 0 \quad \text{at } r = r_o \\ \text{Top/bottom lids:} \quad & u_r = 0, \quad u_\phi = 0, \quad u_z = 0 \quad \text{at } z = 0, H, \end{aligned} \quad (2.8)$$

where a smoothing function  $\psi$  (see section 3) is applied to avoid singularities at  $r = r_i$  and  $z = 0$  or  $z = H$ . These boundary conditions differ from the usually used periodic approximation in the sense that they introduce an explicit  $z$ -dependence even in the mean flow due to constraints on the azimuthal velocity  $u_\phi$  which must satisfy  $u_\phi(r, \phi, 0) = u_\phi(r, \phi, H) = 0$  at the lids.

## 2.2. Response characteristics and boundary-layer thicknesses

The seminal work of Eckhardt, Grossmann, and Lohse (Eckhardt *et al.* 2007) established the foundation for understanding transport dynamics in TC flow. By averaging the azimuthal velocity  $u_\phi$  over a cylindrical surface of height  $H$  and area  $A(r) = 2\pi rH$  coaxial with the rotating cylinders, where  $r_i \leq r \leq r_o$ , they derived equations describing angular momentum transport and kinetic energy dissipation within TC flow under the assumption of periodic boundary conditions at the top and bottom walls. However, for no-slip boundary conditions at the top and bottom lids, an extended approach is required. The azimuthal velocity  $u_\phi$  becomes a function not only of radius  $r$  but also of axial position  $z$  due to the influence of Ekman layers (Czarny *et al.* 2004) and the confinement imposed by the walls limiting vertical extent.

To derive the modified angular-momentum-flux, we consider equations (2.5) and (2.7) under time and area averaging over a cylindrical surface at fixed radius. Following Eckhardt *et al.* (2007), we introduce radial and axial fluxes of angular velocity:

$$\begin{aligned} J_r(r, z) &= r^3 (\langle u_r \omega \rangle_{\phi, t} - \nu \partial_r \langle \omega \rangle_{\phi, t}), \\ J_z(r, z) &= r^3 (\langle u_z \omega \rangle_{\phi, t} - \nu \langle \partial_z (\omega) \rangle_{\phi, t}), \end{aligned} \quad (2.9)$$

where  $\omega \equiv u_\phi/r$  denotes the angular frequency and  $\langle \cdot \rangle_{\phi, t}$  is an average in time as well as in azimuthal direction. Under the assumption that the flow is axisymmetric and statistically stationary, we obtain the following mean azimuthal angular momentum equation:

$$\partial_r J_r(r, z) + \partial_z J_z(r, z) = 0, \quad (2.10)$$

which means, that the flux vector  $(J_r, J_z)$  is divergence-free in the  $(r, z)$ -plane. The average of (2.10) in the vertical  $z$ -direction yields:

$$\partial_r \langle J_r(r, z) \rangle_z + (J_z(r, H) - J_z(r, 0))/H = 0, \quad (2.11)$$

where

$$J_z(r, H) = -\nu r^3 \partial_z \langle \omega \rangle_{\phi, t} \Big|_{z=H}, \quad J_z(r, 0) = -\nu r^3 \partial_z \langle \omega \rangle_{\phi, t} \Big|_{z=0}. \quad (2.12)$$

In the case of periodic axial boundary conditions one obtains  $J_z(r, H) = J_z(r, 0)$ , so that  $\langle J_r(r, z) \rangle_z = \text{const. in } r$  (Eckhardt *et al.* 2007). Here,  $\langle \cdot \rangle_z$  denotes an average in the  $z$ -direction. However, for no-slip end-walls, Ekman boundary layers at  $z = 0$  and  $z = H$  generate axial transport of angular momentum through the top and bottom lids, and  $\langle J_r(r, z) \rangle_z$  is not radially constant anymore. Instead, using equation (2.11), we can obtain the radially constant quantity, which is the radial flux connected by the cumulative axial exchange with the top and bottom plates,

$$\begin{aligned} J^\omega(r) &\equiv \langle J_r(r, z) \rangle_z + \frac{1}{H} \int_{r_i}^r (J_z(r', H) - J_z(r', 0)) dr' \\ &= \langle J_r(r, z) \rangle_z - \frac{\nu}{H} \int_{r_i}^r r'^3 \left[ \partial_z \langle \omega \rangle_{\phi, t} \Big|_{z=H} - \partial_z \langle \omega \rangle_{\phi, t} \Big|_{z=0} \right] dr' \\ &= \text{const. in } r. \end{aligned} \quad (2.13)$$

We also call  $J^\omega(r)$  the total angular momentum flux. It consists of two contributions: the classical radial transport term  $J_r(r, z)$  that appears also in periodic systems, and an additional axial transport term arising from the  $z$ -dependence of the azimuthal velocity induced by the no-slip endwalls. In order to ensure meaningful validation with experiments, the total angular momentum flux  $J^\omega(r)$  will further be normalized by its value in the

conductive flow regime for periodic boundary conditions (Eckhardt *et al.* 2007)

$$J_0^\omega(r) = 2\nu r_i^2 r_o^2 \frac{\omega_i - \omega_o}{r_o^2 - r_i^2}. \quad (2.14)$$

Since  $J^\omega$  is independent of radius (conserved quantity), and  $J^\omega(r_i) = J^\omega(r_o)$  we can relate the velocity gradients at the inner and outer cylinders as follows:

$$\frac{d\langle\omega\rangle_{r,z,t}}{dr} \bigg|_{r_o} = \eta^3 \frac{d\langle\omega\rangle_{r,z,t}}{dr} \bigg|_{r_i} - \frac{1}{r_o^3 H} \int_{r_i}^{r_o} r'^3 \left( \partial_z \langle\omega\rangle_{\phi,t} \bigg|_{z=H} - \partial_z \langle\omega\rangle_{\phi,t} \bigg|_{z=0} \right) dr'. \quad (2.15)$$

We further introduce boundary layer approximations

$$\frac{d\langle\omega\rangle_{r,z,t}}{dr} \bigg|_{r_i} \approx -\frac{\Delta_i}{\delta_i}, \quad \frac{d\langle\omega\rangle_{r,z,t}}{dr} \bigg|_{r_o} \approx -\frac{\Delta_o}{\delta_o}, \quad (2.16)$$

where  $\Delta_i = |\omega_i - \bar{\omega}|$  and  $\Delta_o = |\bar{\omega}|$  are the angular velocity differences between, respectively, the inner ( $\omega_i$ ) and outer ( $\omega_o$ ) walls and the bulk flow ( $\bar{\omega}$ ), and  $\delta_i$  ( $\delta_o$ ) is the viscous boundary layer thickness at the inner (outer) cylinder. From (2.15) and (2.16) we obtain an approximate formulation for the ratio between the outer and inner boundary layer thicknesses,

$$\frac{\delta_o}{\delta_i} = |\bar{\omega}| \left( \eta^3 \Delta_i + \delta_i r_o^{-3} H^{-1} \int_{r_i}^{r_o} r'^3 \left( \partial_z \langle\omega\rangle_{\phi,t} \bigg|_{z=H} - \partial_z \langle\omega\rangle_{\phi,t} \bigg|_{z=0} \right) dr' \right)^{-1}. \quad (2.17)$$

The term in brackets represents the axial correction to the classical periodic prediction (Eckhardt *et al.* 2007), accounting for the  $z$ -dependent flow structure near the endwalls.

### 3. Numerical setup

Direct numerical simulations were conducted with the in-house code **GOLDFISH** (Shishkina *et al.* 2015; Reiter *et al.* 2021, 2022), which has been adapted to account for rotation (Horn & Shishkina 2015; Horn & Schmid 2017; Zhang *et al.* 2020, 2021), internal wall inside the convection container (Shishkina *et al.* 2015; Emran & Shishkina 2020), and different boundary conditions (Ecke *et al.* 2022; Zhang *et al.* 2024), and has been widely used in previous studies of convective flows. **GOLDFISH** employs a fourth-order finite-volume discretization on staggered grids and a third-order Runge–Kutta time-marching scheme.

With the reference length  $r_o$ , reference time  $1/\omega_i$ , and reference velocity  $r_o \omega_i$  the non-dimensionalized governing equations (2.3), under assumption of pure inner cylinder rotation, take the form

$$\begin{aligned} \nabla' \cdot \mathbf{u}' &= 0, \\ \frac{\partial \mathbf{u}'}{\partial t'} + (\mathbf{u}' \cdot \nabla') \mathbf{u}' &= -\nabla' p' + \frac{\kappa}{\sqrt{Ta}} \nabla'^2 \mathbf{u}', \end{aligned} \quad (3.1)$$

where

$$\kappa = \frac{(1 + \eta)^3 (1 - \eta)}{8\eta}.$$

In the following we omit the prime symbols for simplicity.

A significant numerical challenge arises at the junction between the rotating inner cylinder and the stationary top and bottom lids, where the no-slip condition creates a

velocity discontinuity. Without appropriate treatment, this singularity causes numerical instabilities due to extreme velocity gradients. We address this issue by introducing a smooth transition function in the axial direction. Near the lids at  $z = 0$  and  $z = H$ , we modify the azimuthal velocity boundary condition on the inner cylinder:

$$u_\phi(r_i, z) = r_i \omega_i \psi(z, \epsilon), \quad (3.2)$$

where  $\psi$  is a smoothing function and  $\epsilon$  a constant that controls the transition width. In this regard, a sigmoid function has been employed (see section A.1), which minimizes non-physical second derivatives, that affect viscous terms, while ensuring smooth first derivatives.

To ensure reliable numerical results, both temporal and spatial resolution must be sufficiently small to resolve Kolmogorov length and time microscales (Pope 2000). Our first resolution requirement is  $\delta/\eta_K < 1.0$ , where  $\delta = \sqrt[3]{r\delta_\phi\delta_r\delta_z}$  is the local grid spacing and  $\eta_K$  is the Kolmogorov length. Additionally, following Ostilla *et al.* (2013), we check the flatness of the radial profile of the angular momentum flux. Since angular momentum flux should remain constant across the gap width (as derived in section 2), we require the peak-to-peak variation to be below 1%. This criterion, combined with the Kolmogorov-scale resolution, yields the grid configurations used throughout this work. In this study, we were able to achieve sufficient angular momentum flux constancy for all cases presented while also maintaining close adherence to the Kolmogorov criterion (see Appendix A.3).

## 4. DNS results, experimental comparison and boundary layer estimations

### 4.1. Effect of smoothing range

Systematic variation of the smoothing width  $\epsilon$  reveals the following observations. The angular momentum flux exhibits a constant offset across all Reynolds numbers, representing a proportional shift in  $J^\omega$ , while the fundamental flow physics remain unchanged. Figure 2 demonstrates this behavior across the parameter range  $Re \in [50, 700]$  for five different smoothing widths ( $\epsilon = 2\%, 3\%, 5\%, 8\%$  and  $10\%$  of the domain height). A plausible explanation for the constant offset lies in the effective thickening of the Ekman boundary layers near the top and bottom lids. The smoothing zones damp velocity fluctuations in these regions, leading to increased viscous dissipation and reduced turbulent momentum transport. This effect mimics a thicker viscous sublayer, which is known to reduce the efficiency of angular momentum transport in wall-bounded flows (Poncet *et al.* 2013; Leng & Zhong 2022). Since the additional dissipation scales proportionally with the local momentum flux, the relative reduction remains approximately constant across different Reynolds numbers.

We furthermore observe a shift in the onset of Taylor vortex flow in comparison to the experiments chosen for validation. The shift in critical Reynolds number arises because the smoothing function creates artificial rotation of the lids near the junction with the cylinder walls, effectively modifying the boundary conditions (Wendt 1933).

These systematic offsets necessitate appropriate corrections in both Reynolds number and angular momentum flux. We calibrate this effect using the  $\epsilon = 2\%$  case as our reference configuration, which has been chosen to replicate typical experimental conditions (van Gils *et al.* 2011), while maintaining computationally feasible mesh requirements. The observed offsets are purely additive in Reynolds number ( $Re \rightarrow Re + \Delta Re_{\text{offset}}$ ) and purely multiplicative in angular momentum flux ( $J^\omega \rightarrow J^\omega(1 + \epsilon_{\text{offset}})$ ), where  $\Delta Re_{\text{offset}}$  was chosen to be exactly 10% of the Reynolds number value, where convection sets in. This value lies within the bifurcation shift predicted by Wendt (1933) for the aspect ratios

examined in the present study, leading to quantitative agreement with experimental data.  $\epsilon_{\text{offset}}$  has been selected such that our angular momentum flux calculations match the experimental results for Reynolds numbers in the conductive regime of Ostilla *et al.* (2013); Ramesh *et al.* (2019) or Martínez-Arias *et al.* (2014).

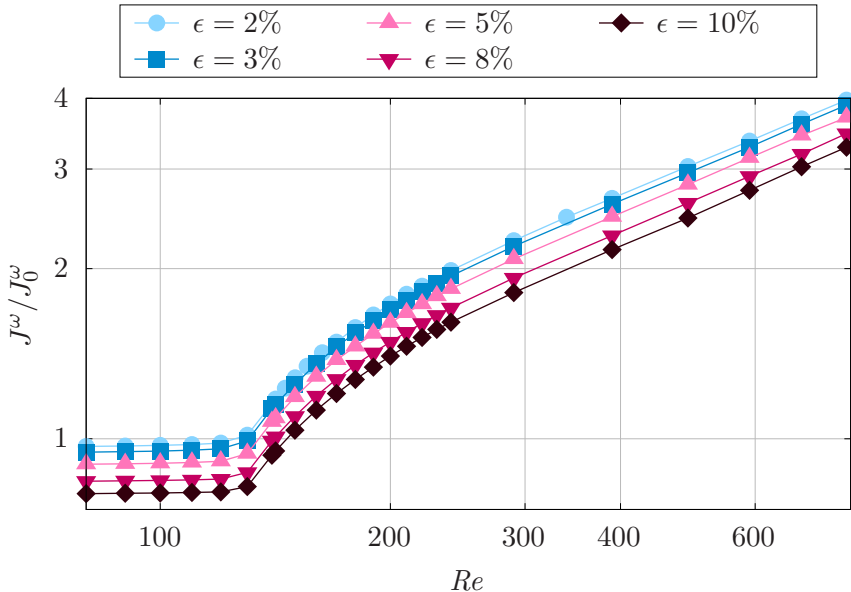


Figure 2. Angular momentum flux development for different smoothing ranges ( $\epsilon = 2\%, 3\%, 5\%, 8\%$  and  $10\%$ ) in the range of  $50 \leq Re \leq 700$  for  $\Gamma = 30$  and  $\eta = 0.909$ .

This procedure enables straightforward systematic corrections that allow consistent comparison with experimental data. Importantly, since these offsets do not affect scaling exponents or the relative locations of regime transitions when properly normalized, the smoothing approach does not alter the fundamental flow physics but merely shifts the absolute values of control and response parameters.

#### 4.2. The role of initial conditions

The choice of initial conditions is crucial in complex hydrodynamic systems exhibiting multiple stable states (Ruelle & Takens 1971; Fenstermacher *et al.* 1979; Wang *et al.* 2020; Yao *et al.* 2025). We have observed significant differences in flow dynamics depending on the initialization procedure, as evidenced by validation of our DNS with the measurements by Martínez-Arias *et al.* (2014) (see Section 4.3).

Simulations initialized with zero velocity fields consistently evolve toward conditionally stable Taylor vortex flow states with asymmetric roll configurations (see figure 3), even at high inner cylinder rotation rates where alternative flow states might be expected. However, by adding white noise perturbations (see section A.1) to these simulation results, we observed significant dynamical shifts. Specifically, systems underwent transitions from Taylor vortex flow (TVF) to wavy vortex flow (WVF) in regimes where WVF has been observed experimentally and predicted theoretically (Martínez-Arias *et al.* 2014).

These observations motivated our initialization strategy for a systematic study of multiple states in TC flow. In our DNS, we initialize the flow with an analytically constructed velocity field that satisfies the continuity equation and boundary conditions while containing the characteristic Taylor vortex structure (see section A.1). This perturbed vortex flow state for

a specific roll configuration serves as the initial condition for our systematic exploration of the multiple states in phase space (for details see section 5).

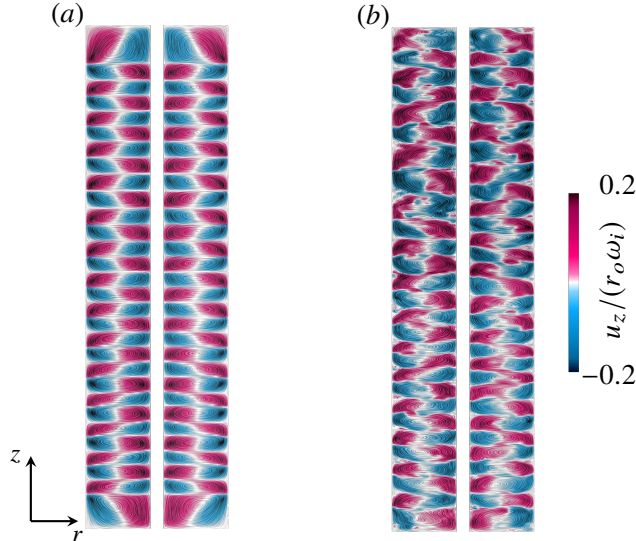


Figure 3. Instantaneous snapshots of axial velocity within the Taylor–Couette system in central vertical cross-sections for  $\Gamma = 30$ ,  $\eta = 0.909$  and different  $Re$  (a)  $Re = 1500$  and (b)  $Re = 4500$ , initialized with  $\mathbf{u}_{\text{initial}} = \mathbf{0}$ . Presented is a TVF state on the left and a WVF state on the right.

The excellent agreement of our angular momentum flux results with experimental data (see section 4.3) validates this initialization procedure.

#### 4.3. Comparison with experiments

We compare our numerical results with two experimental studies: Ramesh *et al.* (2019) and Martínez-Arias *et al.* (2014). These experiments employ different geometric parameters and significantly different aspect ratios, providing complementary validation across distinct parameter regimes. Figures 4 and 6 show the comparisons with both experimental measurements. Due to the smoothing function described in section 3, we apply systematic corrections to match the experimental data. A 10% shift in Reynolds number and a specific geometry dependent prefactor in the angular momentum flux were used for calibration such that the difference in angular momentum flux measurements in the laminar regime remains below 1%.

We first compare our DNS results with the measurements of Ramesh *et al.* (2019) for  $\eta = 0.914$  and  $\Gamma = 11$ . Figure 4 demonstrates good agreement with the experimental results regarding both the onset of Taylor vortex flow and the subsequent angular momentum flux evolution. The development of the flow field dynamics (depicted in figure 5) supports the description by Ramesh *et al.* (2019) regarding the physical mechanisms responsible for the shift in the critical Reynolds number compared to theoretical estimates of  $Re_c = 142.15$  (Di Prima & Swinney 1981) for infinitely long cylinders. The transition to TVF occurs at lower  $Re$  than predicted by linear stability theory due to perturbations induced by Ekman vortices (Ramesh *et al.* 2019). Our flow visualizations clearly reveal the early self-organization of convection rolls in the vicinity of the lids, which progressively penetrate deeper into the flow domain as  $Re$  increases. However, a significant increase in the discrepancy between simulation and experiment can be observed at the upper end of

the Reynolds number range. This deviation is most likely due to the formation of roll configurations that differ from those measured in the experiments and will be further discussed in chapter 5.

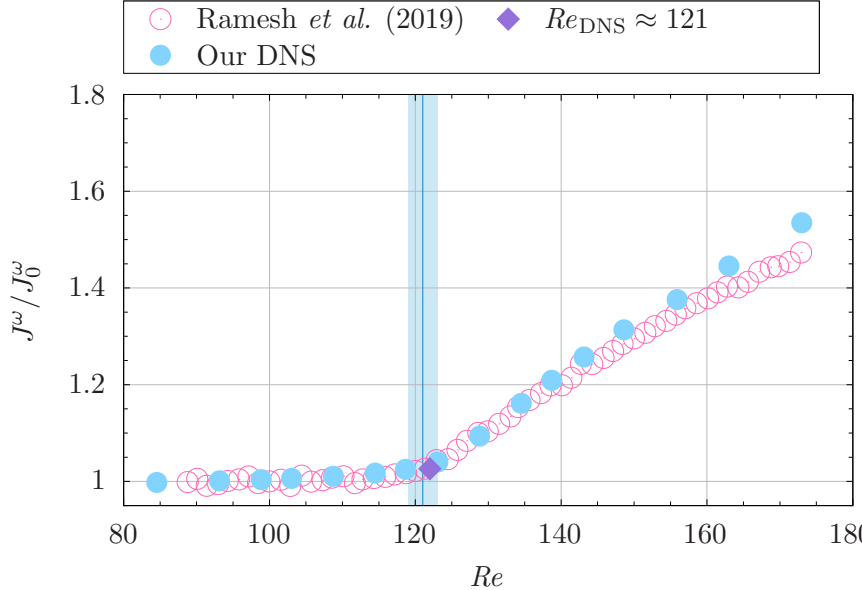


Figure 4. Angular momentum flux development for moderate  $Re$  values in the setup of Ramesh *et al.* (2019) for  $\Gamma = 11$ ,  $\eta = 0.914$ . The blue region highlights the onset of convection in the experiments, which agrees perfectly with our simulation result ( $\blacklozenge$ ). The earlier transition in comparison to the periodic assumption is due to perturbations by Ekman vortices (see figure 5).

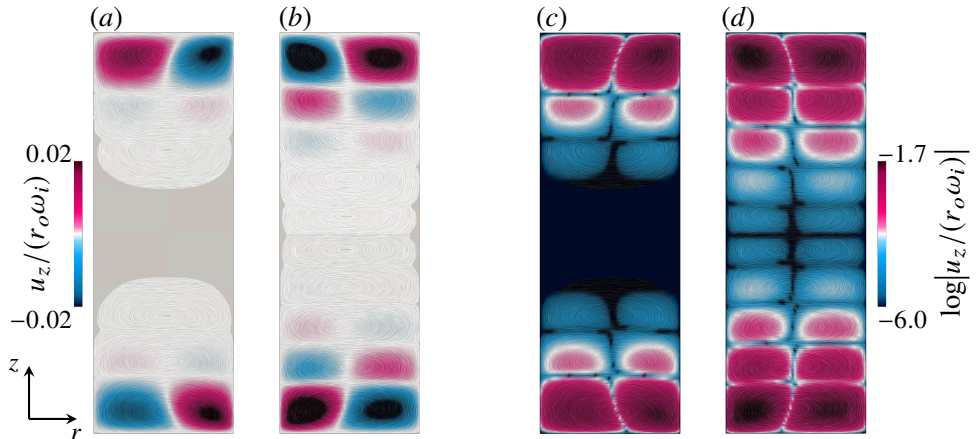


Figure 5. Central vertical cross-sections of the instantaneous vertical velocity for two different Reynolds numbers (a, c)  $Re = 90$  and (b, d)  $Re = 120$  in the setup of Ramesh *et al.* (2019) for  $\Gamma = 11$  and  $\eta = 0.914$ . The colour coding resolves the strength in axial velocity in (a, b), where blue (red) denotes negative (positive) velocities. Smooth contiguous regions indicate areas below the filter threshold of  $10^{-6}$ . In (c, d) the amplitude of the axial velocity is shown on a logarithmic scale ranging from lower (blue) to higher (red) velocities to enhance the contrast in roll-configuration visibility. (a, c) At  $Re = 90$ , convection rolls form initially from the upper and lower boundaries and penetrate into the centre of the domain. Due to the limited angular frequency of the inner wall, the roll formation cannot yet cover the full domain. (b, d) At  $Re = 120$ , the external driving is strong enough to enable a domain-wide convection roll development.

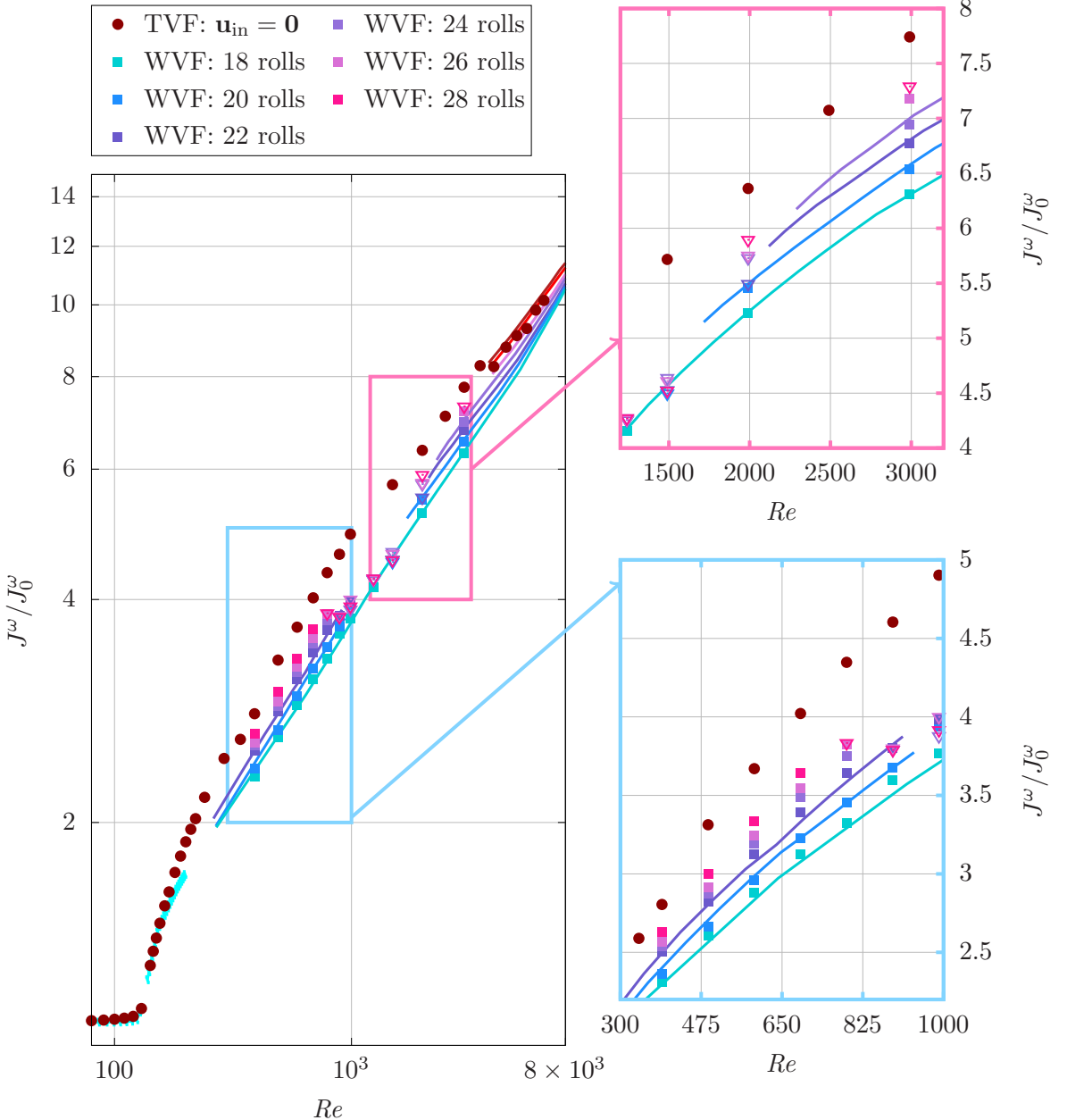


Figure 6. Angular momentum flux development for  $50 \leq Re \leq 8 \times 10^3$  in the setup with  $\Gamma = 30$  and  $\eta = 0.909$ . Solid lines denote the experimental data by Martínez-Arias *et al.* (2014) and symbols our DNS data for different stable roll configurations. Brown circles show our DNS results for zero initial velocity, whereas coloured squares (triangles) show our DNS results of multiple persistent (non-persistent) state simulations with an initial velocity specifically chosen in regard of the respective roll configuration (see section A.1). We can highlight an excellent agreement with the experimental results for the multiple states phase space region, with a reduction of possible persistent configurations between  $800 < Re < 2 \times 10^3$  and a sudden regrowth of the accessible phase space volume for higher  $Re$ . This transition can be understood by analysing the transition in the flow dynamics with rising  $Re$ . Closer views are shown on the right figures.

Another experimental study we compare with is by Martínez-Arias *et al.* (2014) for a system with significantly different geometry ( $\eta = 0.909$  and  $\Gamma = 30$ ). Figure 6 shows a pronounced quantitative agreement between our DNS results (coloured symbols) and their experimental data (coloured lineplots) across the full range of  $50 \leq Re \leq 5000$ . Our simulations with different initial roll numbers (18, 20, 22, 24, 26, and 28 rolls) all converge to the corresponding experimental curves in stable regimes, validating our numerical approach.

We also observe pronounced differences in flow dynamics depending on initial conditions. Simulations initialized with zero velocity fields and  $Re \leq 4000$  consistently evolve toward conditionally stable Taylor vortex flow states with asymmetric roll configurations. However, higher Reynolds numbers impose sufficient disturbances to drive the system out of the Taylor-Vortex attractor towards more wavy or modulated vortex states. By adding white noise perturbations to the initial velocity field, we observed significant dynamical shifts. Specifically, systems underwent transitions from TVF to WVF in regimes where WVF has been observed experimentally. This observation motivated the initialization procedure described in section A.1, whereby we initialize the system with disturbed Taylor vortex flow of the desired roll number. This approach enabled us to systematically study the occurrence and dynamics of multiple states while maintaining excellent agreement with experimental measurements (for detailed discussion on multiple states see section 5).

#### 4.4. Boundary layer theory with axial corrections

To examine the spatial structure in detail, figure 7 shows radial profiles of the averaged angular velocity  $\langle u_\phi \rangle_{\phi, z, t}$  for different Reynolds numbers. At low  $Re$ , the monotonic profiles exhibit clear boundary layers near both cylinders with a weakly changing bulk region. At higher  $Re$ , the steeper gradients near the walls reflect the increased importance of turbulent fluctuations in momentum transport.

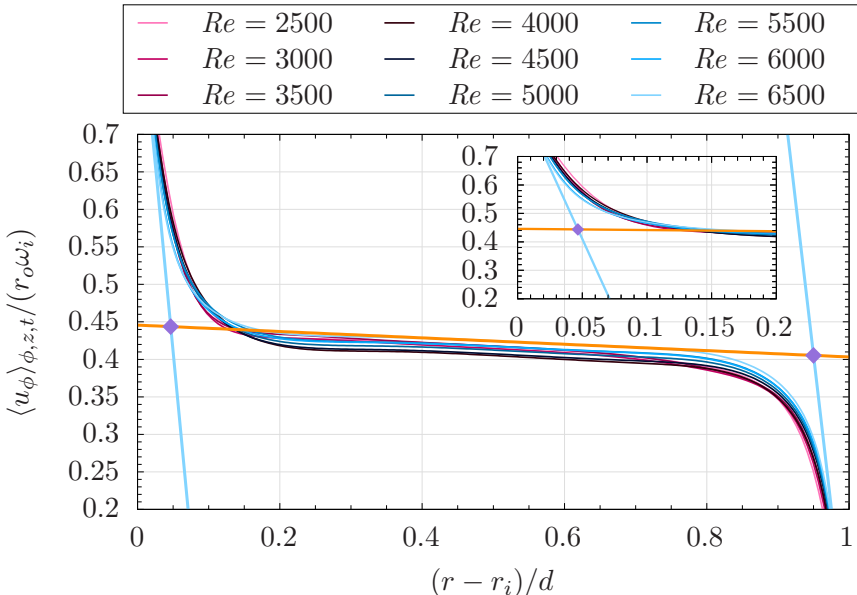


Figure 7. Sketch of the boundary layer thickness estimation for  $2.5 \times 10^3 \leq Re \leq 6.5 \times 10^3$  in the setup of Martínez-Arias *et al.* (2014) for  $\Gamma = 30$  and  $\eta = 0.909$ . Violet diamonds denote the estimated width of the boundary layer obtained via the slope method: linear fits to the two wall-most points are extrapolated to intersect a horizontal line at the bulk angular velocity.

Using the extended angular momentum flux formulation validated above, we now examine boundary layer structure and compare our DNS results with theoretical predictions. A key quantity for characterizing flow asymmetry is the ratio of outer to inner boundary layer thicknesses,  $\delta_o/\delta_i$ . Figure 8 presents this ratio as a function of  $\sqrt{Ta}$ . The DNS data are compared with the extended theory including axial corrections (cyan squares in figure 8) as introduced in section 2, and the periodic boundary approximation (magenta triangles) representing Eckhardt *et al.* (2007) predictions that neglect axial transport. Figure 8 reveals several important features. As shown in figure 6, simulations at  $Re < 4000$  consistently evolve toward a stable TVF state. Within this laminar to weakly nonlinear regime, the boundary-layer thickness ratio  $\delta_o/\delta_i$  exceeds unity and grows with increasing  $Ta$ , reflecting the stronger mean shear at the rotating inner cylinder relative to the stationary outer wall. Upon transition to WVF, the ratio drops significantly. This behavior is attributed to coherent wave structures that preferentially enhance angular momentum transport toward the outer cylinder. Consequently, the outer boundary layer thins significantly, while the inner boundary layer, which is already governed by the imposed rotational shear, remains largely unaffected. This results in a reduction of the thickness ratio. The predicted boundary layer ratio based on equation (2.17) consistently underestimates the DNS results. This underestimation also increases with higher  $Ta$  due to steeper radial gradients of  $\omega$ , which are not sufficiently captured by our linear approximation (2.16).

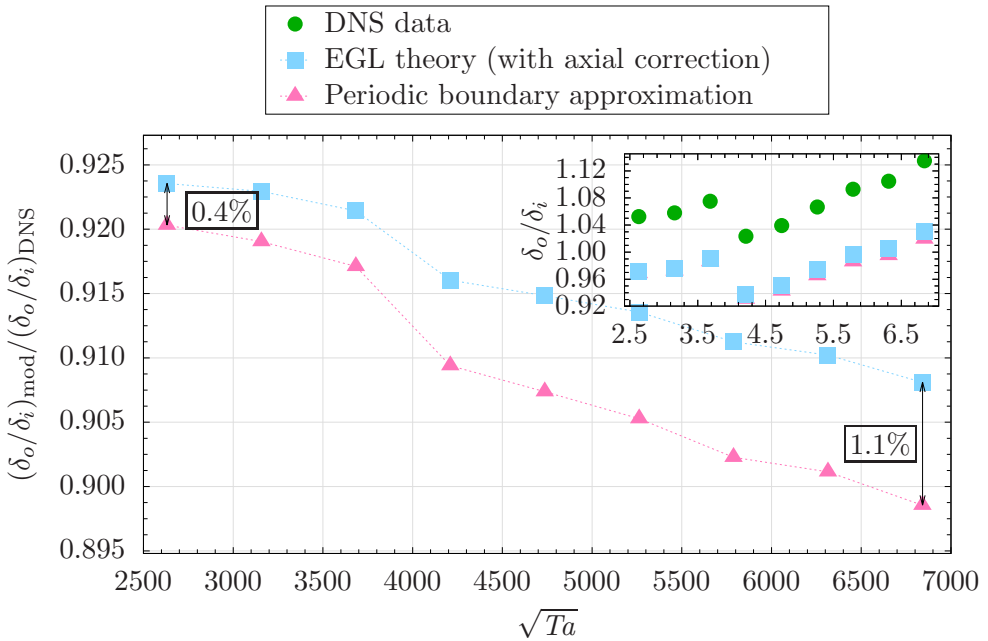


Figure 8. Ratio of the boundary layer thicknesses based on theoretical predictions compared to the ones obtained in the DNS for  $2.5 \times 10^3 < \sqrt{Ta} < 7 \times 10^3$  in the setup of Martínez-Arias *et al.* (2014) for  $\Gamma = 30$  and  $\eta = 0.909$ . Shown is the model predicted ratio (2.17) against the DNS results estimated based on the procedure shown in figure 7. The inset in the top right corner shows the non-normalized ratios against  $\sqrt{Ta} \times 10^{-3}$ . The deviation between modified theory and periodic approximation grows significantly with higher  $Ta$ .

Interestingly, we also observe a significant increase in the deviation between the periodic approximation and the modified model for higher rotation rates of the inner cylinder. This finding is consistent with our angular momentum flux analysis shown in section A.2,

highlighting the dependence of endwall boundary layer effects as a function of  $Ta$ . The corrections introduced by the additional term in equation (2.17) are therefore quantitatively significant and cannot be neglected for accurate predictions in realistic geometries.

## 5. Multiple stable states and hysteresis

To systematically explore the stability landscape, we performed DNS runs at Reynolds numbers  $Re \in \{400, 3000\}$ , in the setup of  $\Gamma = 30$  and  $\eta = 0.909$ , with initial conditions covering different roll number configurations  $n \in \{18, 20, 22, 24, 26, 28\}$ , based on the experimental findings by Martínez-Arias *et al.* (2014). Each simulation was run for sufficient time to determine the final persistent state, typically exceeding 600 rotational time units ( $t_{\text{rot}} = t\omega_i$ ). Our simulations reveal that multiple distinct stable states can coexist at identical Reynolds numbers, with the final roll number depending sensitively on the initial condition. However, we also observe the occurrence of additional stable states not reported in their experimental work. This discrepancy likely arises because numerical simulations are significantly less susceptible to external perturbations than experimental investigations. It should be noted, however, that some configurations may require longer integration times to fully capture potential transitions to lower roll numbers.

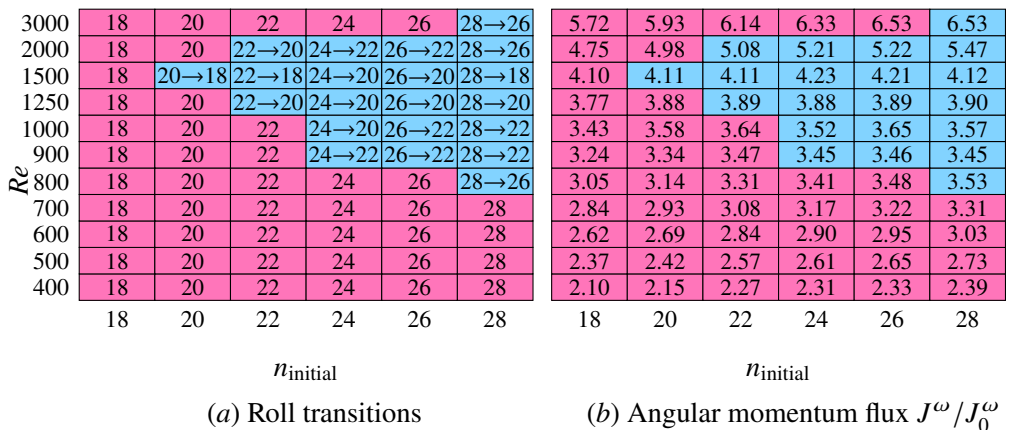


Figure 9. Roll stability map for  $400 \leq Re \leq 3 \times 10^3$  in the setup of Martínez-Arias *et al.* (2014) for  $\Gamma = 30$  and  $\eta = 0.909$ . (a) Stable (pink) versus unstable (blue) configurations with initial and final number of rolls. (b) Corresponding normalized angular momentum flux  $J^\omega/J_0^\omega$  for each configuration. Note that after surpassing the chaotic wavy vortex flow regime, more rolls regain their stability.

Figure 6 illustrates the occurrence of multiple states across the investigated Reynolds number range. The presented phase space exhibits distinct regimes with qualitatively different behavior. At low Reynolds numbers ( $Re < 900$ ), multiple stable states coexist, and the final state depends on initialization, indicating a hysteresis region with significant accessible phase space volume. In the lower intermediate regime ( $900 < Re < 1250$ ), the system converges to a single state, but with fewer rolls than at low  $Re$ , suggesting roll merging events. The upper intermediate regime ( $1250 < Re < 2000$ ) exhibits unique final states regardless of initial conditions, representing a region of strong convergence. At high Reynolds numbers ( $Re > 2500$ ), we observe a remarkable regrowth of the accessible phase space region for possible roll configurations. This phenomenon is of particular interest. As described in the work of Dutcher & Muller (2009), the expansion of accessible phase space at high  $Re$  highlights the crucial role of flow dynamics in determining the stability

of respective flow patterns. The system undergoes a cascade of transitions from TVF through WVF, modulated wavy vortex flow (MWF), chaotic wavy vortex flow (cWVF), turbulent wavy vortex flow (tWVF), to turbulent Taylor–vortex flow (tTVF). This cascade provides insight into the regrowth dynamics. At sufficiently high Reynolds numbers, turbulence might suppress or dissolve secondary instabilities, therefore restabilizing large-scale coherent structures. Additionally, no-slip boundary conditions preferentially stabilize roll structures near the endwalls, including another persistent stabilization effect across several  $Re$ -regimes even in otherwise turbulent flow (see Ramesh *et al.* (2019) and section 5.2 for detailed flow structure analysis).

The stability map (figure 9) clearly delineates persistent (magenta) and non-persistent (cyan) regions in  $(Re, n_{\text{initial}})$  space. The embedded numbers show the actual roll numbers achieved after the system reaches statistical steady state, revealing the complex structure of the attractor landscape. Persistent configurations (appearing as magenta regions in figure 9 *a*), indicate that certain  $(Re, n_{\text{initial}})$  combinations are absolutely stable and resist perturbations. Reduction channels manifest as cyan regions showing systematic roll number reduction through merging events. Furthermore, critical boundaries separate persistent and non-persistent configurations with sharp transitions, suggesting that the system exhibits bifurcation-like behavior at these interfaces.

### 5.1. Roll aspect ratio effect on transport

Following Martínez-Arias *et al.* (2014), we investigated the scaling of angular momentum flux with Taylor number for different roll configurations. Our results (see figures 6 and 10) highlight that the angular momentum flux efficiency increases with the number of rolls in the investigated Taylor number range, consistent with theoretical expectations. This behaviour differs from that observed in the ultimate regime (Martínez-Arias *et al.* 2014).

Our analysis also demonstrates that different roll states exhibit distinct scaling exponents  $\alpha$  in the relationship  $J^\omega \propto Ta^\alpha$ .

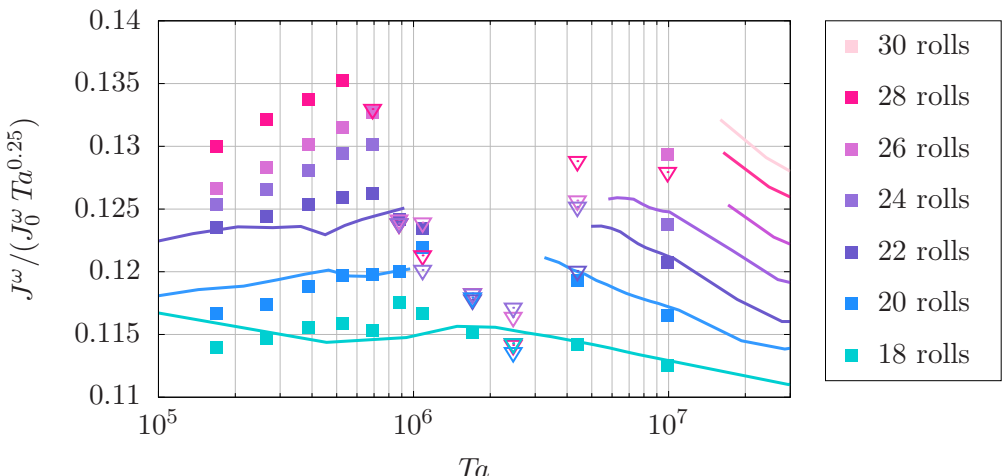


Figure 10. Angular momentum flux development for  $10^5 \leq Ta < 3 \times 10^7$  in the setup with  $\Gamma = 30$  and  $\eta = 0.909$  normalized by  $Ta^{0.25}$ . Solid lines denote the experimental data by Martínez-Arias *et al.* (2014) for different stable roll configurations. Coloured squares (triangles) show our DNS results of multiple persistent (non-persistent) states. Colours were chosen as in figure 6.

This finding is consistent with previous studies that identified the dependence of the proportionality coefficient on the aspect ratio of individual rolls (Froitzheim 2019). Interestingly, this behavior differs from that observed in DNS of two-dimensional Rayleigh–Bénard convection, where the scaling exponent remained invariant across different roll configurations (Wang *et al.* 2020). Beyond the inherent differences between 3D and 2D flow structures, the difference may arise from the additional geometric constraints imposed by the cylindrical geometry and the no-slip endwalls in Taylor–Couette systems, which break the strict two-dimensional symmetry present in idealized 2D Rayleigh–Bénard configurations with periodic side walls. This systematic variation of the transport scaling with roll configuration provides direct evidence that the aspect ratio of coherent structures, and not only the global Reynolds number, plays a fundamental role in determining turbulent transport efficiency in Taylor–Couette flow.

## 5.2. Transition dynamics and energy budget analysis

To gain deeper insight into the mechanisms governing transitions between different roll configurations, we analyze the temporal evolution of unstable states and quantify the energy transfer between dominant flow modes.

### 5.2.1. Space-time dynamics of unstable configurations

Figure 11 shows space-time diagrams of the axial velocity component  $u_z(r, \phi, z, t)$  at mid-gap radius and  $\phi = 0$  for two different configurations. These diagrams provide valuable insight into the characteristic evolution of roll merging events and allow for systematic tracking of the temporal dynamics.

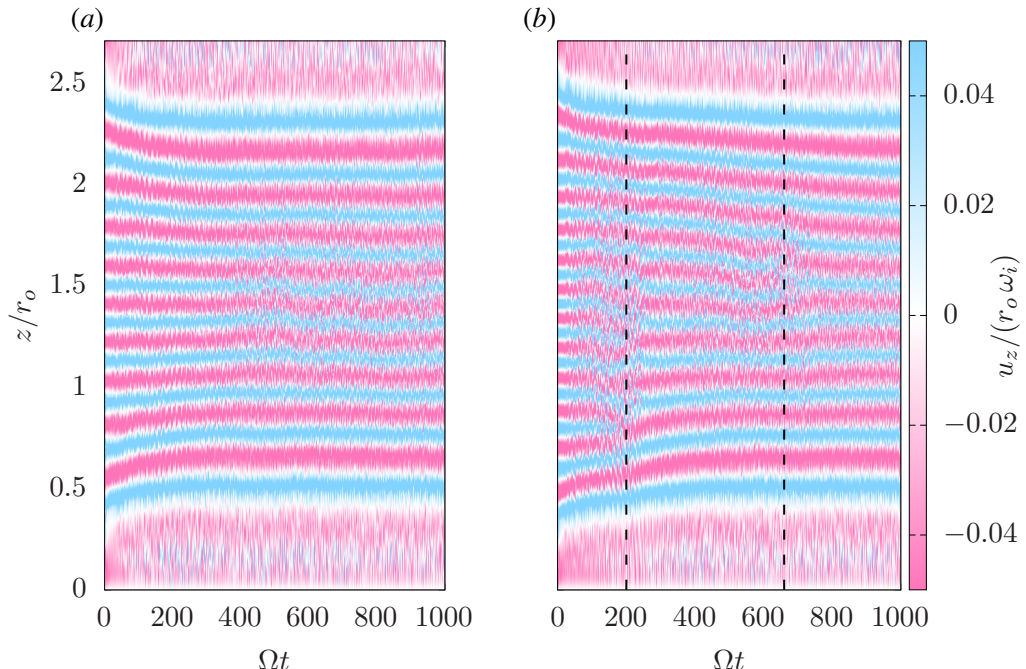


Figure 11. Space–time diagrams for two different initial roll developments in the setup of Martínez-Arias *et al.* (2014) for  $\Gamma = 30$  and  $\eta = 0.909$ . Shown is the normalized axial velocity  $u_z$  at mid-gap radius and  $\phi = 0$ . (a) Persistent configuration for  $Re = 1250$  and  $n_{\text{initial}} = 20$ . (b) Non-persistent initialisation  $Re = 1250$ ,  $n_{\text{initial}} = 26$  with pronounced roll merging occurrences highlighted by the dotted lines.

In contrast to persistent configurations, which exhibit stationary horizontal bands with consistent spacing (figure 11a), non-persistent states (figure 11b) display pronounced diagonal features indicating temporal evolution of the roll structures and their progressive reorganization.

We observe systematic merging events occurring over extended timescales of  $\Delta t \approx 200$  to 400 rotation periods, demonstrating the relatively slow nature of these instability-driven transitions. The merging process proceeds through well-defined stages that can be clearly identified in the space-time diagrams. Two neighboring rolls, rotating in the same direction, gradually approach each other axially over time, the interface between them progressively weakens and becomes increasingly diffuse until the two rolls coalesce into a single, larger vortex structure with reduced angular momentum transport. This process continues iteratively until the system reaches a stable configuration with fewer rolls and increased axial wavelength.

The spatial location of merging events is not random but shows clear preferential occurrence away from the endwalls, where no-slip boundary conditions and geometric constraints stabilize present roll flow structures and suppress local instabilities. This observation aligns with our earlier discussion (section 4.3) regarding the crucial role of realistic boundary conditions in determining flow evolution and the importance of resolving endwall effects accurately.

### 5.2.2. Modal energy transfer during roll merging

To quantify the energy redistribution during transitions, we perform azimuthal Fourier decomposition of the velocity field. The analysis is restricted to the radial velocity component, which exhibits the strongest signature of the vortex roll dynamics and azimuthal waviness,

$$u_r(r, \phi, z, t) = \sum_{m=0}^M \hat{u}_{r,m}(r, z, t) e^{im\phi}, \quad (5.1)$$

where  $m$  is the azimuthal wavenumber and  $M$  is the maximum wavenumber considered in the truncated Fourier series.

We further compute the radial fraction of the kinetic energy associated with each mode:

$$E_{r,m}(t) = \frac{1}{2H} \int_z |\hat{u}_{r,m}|^2 \Big|_{r=\frac{r_i+r_o}{2}, \phi=0} dz. \quad (5.2)$$

Figure 12 shows the energy distribution among azimuthal modes for four persistent roll configurations at different  $Re$ , together with the corresponding axial profiles of  $u_r$ . Table 1 presents the energy fractions carried by the axisymmetric mode ( $m = 0$ ) and non-axisymmetric modes ( $m > 0$ ), respectively. At  $Re = 800$ , the flow exhibits weak wavy vortex flow (WVF), with the axisymmetric mode dominant and only one additional azimuthal mode weakly excited. At  $Re = 1250$ , the azimuthal modulation intensifies significantly, with non-axisymmetric modes now carrying more energy than the previously dominant  $m = 0$  mode. At  $Re = 2000$ , a resurgence of the axisymmetric mode is observed, with  $m = 0$  regaining dominance. This re-emergence of axisymmetric structure in the turbulent regime is consistent with the observations of Dutcher & Muller (2009), who described a cascade of transitions from WVF through modulated wavy vortex flow (mWVF) and chaotic wavy vortex flow (cWVF) towards turbulent wavy vortex flow (tWVF).

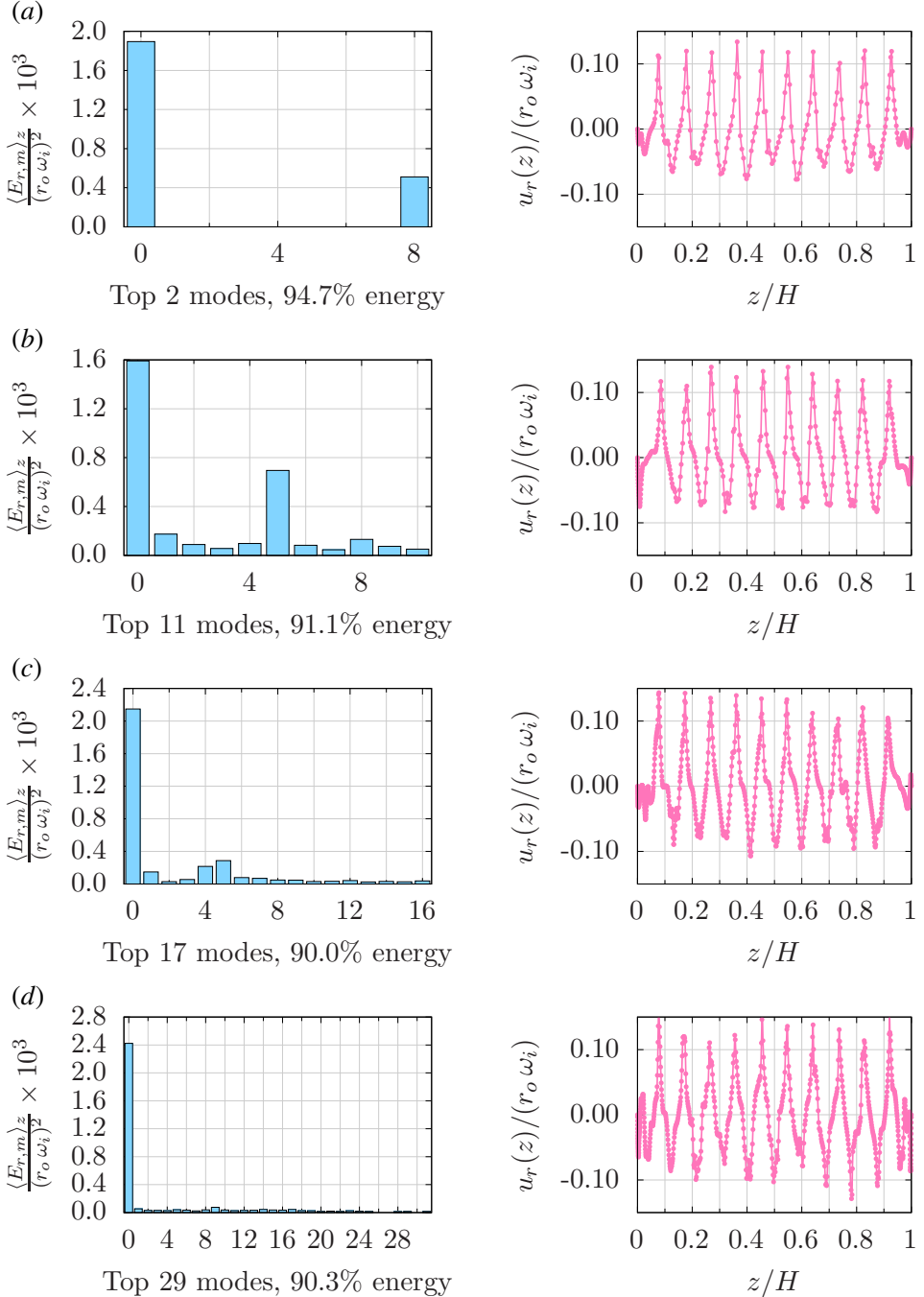


Figure 12. Mode decompositions of the radial kinetic energy fraction in the setup of Martínez-Arias *et al.* (2014) for  $\Gamma = 30$ ,  $\eta = 0.909$  and  $n = 20$ , as obtained in the DNS for (a)  $Re = 800$  (b)  $Re = 1250$  (c)  $Re = 2000$  (d)  $Re = 3000$ . Axial profiles of the normalized radial velocities for the respective cases are shown on the right.

$Re$	$m = 0$ (%)	$m > 0$ (%)
800	74.5	25.5
1250	46.9	53.1
2000	67.2	32.8
3000	60.5	39.5

Table 1. Energy fractions of zeroth- and higher-order modes

Our findings support this interpretation: the corresponding phase space analysis reveals that the stability region contracts and expands in correlation with these transitions, suggesting that variations in azimuthal waviness directly influence the extent of the persistent parameter space.

Figure 13 displays the temporal evolution of modal energy fractions for a representative transition case ( $Re = 1250$ ,  $n_{\text{initial}} = 26 \rightarrow n_{\text{final}} = 20$ ). Several key features emerge from this analysis. The axisymmetric mode ( $m = 0$ ) remains dominant throughout the transition, which reflects the persistence of the basic vortex structures even during reorganization. However, non-axisymmetric modes ( $m > 0$ ) exhibit transient amplification during merging events, emphasized by the dotted lines in figures 11 and 13, while the dominant non-axisymmetric mode shifts during the transition process. This highlights that different roll configurations in the given setup might also lead to a different distribution of excited frequencies in the regard of secondary instabilities. Finally, after the transition completes, the modal energy distribution reaches a new equilibrium corresponding to the final roll configuration. Interestingly, each transition event is preceded by a reduction in the 0-mode's energy fraction, indicating that the system draws energy from the base flow to realize configurational changes. This phenomenon could serve as a predictor for transition scenarios and will be part of future work.

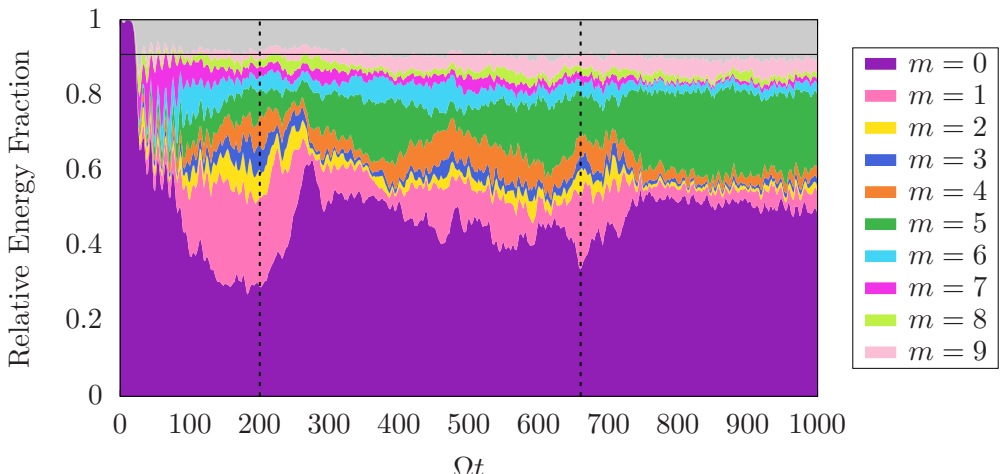


Figure 13. Energy distribution development for  $Re = 1250$ ,  $n_{\text{init}} = 26$  in the setup of Martínez-Arias *et al.* (2014). The top 10 modes, which together cover over 90% of the system's total energy budget, are shown with distinct colours. In this non-persistent configuration, several energy shifts occur and subsequently push the system into another configuration scheme. Dotted lines highlight completed roll merging events as shown in figure 11.

## **6. Conclusions**

We have performed a DNS study of Taylor–Couette flow with realistic no-slip boundary conditions at all surfaces. In this study, we extended the classical periodic angular momentum flux formulation by Eckhardt *et al.* (2007) to include axial transport terms arising from  $z$ -dependent azimuthal velocity. This modification yields spatially constant angular momentum fluxes and improved boundary layer predictions.

The wall-lid singularity inherent in this configuration requires careful treatment via smoothing functions. We demonstrated that sigmoid smoothing provides numerical stability while introducing only a constant offset in angular momentum flux that can be systematically corrected. Excellent quantitative agreement with experimental data from Martínez-Arias *et al.* (2014) and Ramesh *et al.* (2019) validates our DNS approach and confirms the experimental relevance of the simulated flow structures.

A systematic parameter space exploration revealed coexistence of multiple stable flow states with different roll numbers at identical Reynolds numbers. Stability diagrams provide a foundation for future investigations into the detailed mechanisms governing state selection and transitions. The system exhibits strong hysteresis, with the final state depending on initial conditions. This multistability arises from competing length scales, Ekman layer effects, and finite-size disturbances, wherein different roll configurations interact distinctly with endwall boundary layers, creating separate attractors in phase space.

The existence of multiple stable states with different transport efficiencies has important implications for both fundamental understanding and practical applications. From a fundamental perspective, it demonstrates that Taylor–Couette flow, even with fully deterministic governing equations and fixed control parameters, does not possess a unique turbulent state. Rather, the system exhibits history-dependent behavior, with the initial conditions determining which attractor is realized. From a practical perspective, this multistability presents opportunities for flow control. Preferential selection of states with higher transport efficiency (typically those with more smaller rolls) could optimize industrial mixing processes or heat transfer applications. Conversely, understanding which perturbations trigger transitions between states could help prevent undesired regime changes in sensitive applications. Future work will focus on identifying the physical mechanisms governing transitions between multiple states in Taylor–Couette flow and their relevance to other complex hydrodynamic systems.

## **Acknowledgments**

We truly appreciate the many fruitful discussions with D. Lohse, G. Vacca and H. Dave during the course of this work. Experimental validations were made possible by the support of M. Alam, J. Peixinho and P. Ramesh, who kindly shared their measurement data with us. We further acknowledge financial support from German Research Foundation (DFG) under grants Sh405/20, Sh405/22 and SO2399/2. The presented numerical investigations were enabled by the supercomputing clusters of the Max Planck Computing and Data Facilities.

## Appendix

### A.1. Flow field initialization

To initialize DNS with a Taylor vortex flow that satisfies no-slip boundary conditions at the endplates, and the continuity equation is not trivial. Therefore, we prioritize the exact enforcement of no-slip boundary conditions at the endplates, accepting a minor deviation from perfect divergence-free conditions of the initial flow field, which is localized to the narrow smoothing regions (2% of the domain height at each boundary). Thus the initial field consists of a base Couette flow with superimposed Taylor vortex perturbations. The velocity components in cylindrical coordinates  $(r, \varphi, z)$  are given by:

$$u_\varphi(r, z) = S_z(z) \left[ \frac{\eta^2}{\eta^2 - 1} \left( r - \frac{1}{r} \right) - \frac{A}{2} F(r) \sin(\Phi) \right], \quad (6.1)$$

$$u_r(r, z) = \frac{A}{r} n \pi F(r) S_z(z) \frac{dz'}{dz} \sin(\Phi), \quad (6.2)$$

$$u_z(r, z) = \frac{A}{r} \frac{dF}{dr} S_z(z) \cos(\Phi), \quad (6.3)$$

where  $\eta = r_i/r_o$ ,  $A = 0.05\eta^2$  is the perturbation amplitude, and  $n$  is the number of imposed rolls. The phase function is defined as

$$\Phi(z) = n\pi z'(z) - \frac{\pi}{2}, \quad (6.4)$$

with a simple axial coordinate transformation  $z'(z)$  described below. The radial shape function  $F(r)$  ensures no-slip conditions at both cylinder walls. We employ

$$F(r') = r'^2(1 - r')^2, \quad \text{with} \quad r' = \frac{r - \eta}{1 - \eta}, \quad (6.5)$$

whose derivative is

$$\frac{dF}{dr} = \frac{2r'(1 - r')(1 - 2r')}{1 - \eta}. \quad (6.6)$$

This choice guarantees that both  $F$  and  $dF/dr$  vanish at  $r' = 0$  (inner cylinder) and  $r' = 1$  (outer cylinder), thereby satisfying  $u_r = u_z = 0$  at both walls. To impose no-slip conditions at the endplates ( $z = 0$  and  $z = H$ ), we introduce a sigmoid-based smoothing function with min-max-normalization

$$S_z(z) = \frac{M_{\text{down}}(z) \cdot M_{\text{up}}(z) - \min}{\max - \min}, \quad (6.7)$$

where

$$M_{\text{down}}(z) = \frac{1}{1 + \exp[(z - z_{0,\text{down}})/\epsilon]}, \quad (6.8)$$

$$M_{\text{up}}(z) = \frac{1}{1 + \exp[-(z - z_{0,\text{up}})/\epsilon]}. \quad (6.9)$$

Here,  $\epsilon = 0.02H$  defines the boundary layer thickness (2% of the domain height), and  $z_{0,\text{down}} = 0.01H$  and  $z_{0,\text{up}} = 0.99H$  are the transition centers. The terms  $\min$  and  $\max$  denote the minimum and maximum of  $M_{\text{down}}(z)M_{\text{up}}(z)$  over  $z \in [0, H]$ , which rescales

the smoothing function to  $S_z(z) \in [0, 1]$ . After normalization, we explicitly set  $S_z(0) = S_z(H) = 0$ , ensuring that all velocity components vanish at the endplates. For uniformly sized vortex rolls along the axial direction, we employ a simple linear mapping

$$z'(z) = \frac{z}{H}, \quad (6.10)$$

which distributes all  $n$  vortex rolls equally over the domain height  $H$ .

The constructed velocity field satisfies the following boundary conditions:

$$\begin{aligned} \text{Inner cylinder } (r = r_1): \quad u_r = 0, \quad u_\phi = S_z(z)\eta, \quad u_z = 0 \quad \text{at } r = r_1, \\ \text{Outer cylinder } (r = r_2): \quad u_r = 0, \quad u_\phi = 0, \quad u_z = 0 \quad \text{at } r = r_2, \\ \text{Top, bottom lids } (z = 0, z = H): \quad u_r = 0, \quad u_\phi = 0, \quad u_z = 0 \quad \text{at } z = 0, H. \end{aligned} \quad (6.11)$$

The azimuthal velocity at the inner cylinder reproduces the exact Couette profile

$$u_\phi(r = \eta, z) = S_z(z)\eta = S_z(z)\omega_1 r_1, \quad (6.12)$$

modulated by the axial smoothing function to satisfy the no-slip condition at the endplates. The radial and axial velocity components are derived from a stream function  $\psi(r, z) = AF(r)S_z(z)\cos(\Phi)$  via

$$u_r = \frac{1}{r} \frac{\partial \psi}{\partial z}, \quad u_z = -\frac{1}{r} \frac{\partial \psi}{\partial r}, \quad (6.13)$$

which, under the approximation that  $\frac{dS(z)}{dz}$  is negligible for the majority of the domain, automatically satisfies the continuity equation

$$\nabla \cdot \mathbf{u} = \frac{1}{r} \frac{\partial(ru_r)}{\partial r} + \frac{\partial u_z}{\partial z} = 0. \quad (6.14)$$

To trigger the transition to wavy vortex flow or turbulent states, we add white noise to the initial velocity field. To ensure that the perturbed field remains almost divergence-free, we employ a stream function approach for the radial and axial velocity components, while the azimuthal component is perturbed independently. We introduce a random stream function  $\vartheta$  and its spatial derivatives at each grid point  $(j, k, i)$ :

$$\vartheta_{ki} \propto \mathcal{U}(-\zeta\eta, \zeta\eta), \quad (6.15)$$

$$\left( \frac{\partial \vartheta}{\partial r} \right)_{ki} \propto \mathcal{U}(-\zeta\eta, \zeta\eta), \quad (6.16)$$

$$\left( \frac{\partial \vartheta}{\partial z} \right)_{ki} \propto \mathcal{U}(-\zeta\eta, \zeta\eta), \quad (6.17)$$

where  $\zeta = 0.01$  is the noise intensity (1% of the characteristic velocity  $\eta$  in the non-dimensionalized setting), and  $\mathcal{U}(a, b)$  denotes a uniform distribution on the interval  $[a, b]$ . The noise is then applied to the velocity components as:

$$u_r^{(\text{noisy})}(j, k, i) = u_r(j, k, i) - \frac{1}{r} \frac{\partial \vartheta}{\partial z}, \quad (6.18)$$

$$u_z^{(\text{noisy})}(j, k, i) = u_z(j, k, i) + \frac{1}{r} \frac{\partial \vartheta}{\partial r}, \quad (6.19)$$

$$u_\varphi^{(\text{noisy})}(j, k, i) = u_\varphi(j, k, i) + \xi_{jki}, \quad (6.20)$$

where  $\xi_{jki} \propto \mathcal{U}(-\zeta\eta, \zeta\eta)$  is an independent random perturbation for the azimuthal component. This stream function formulation automatically satisfies the incompressibility constraint  $\nabla \cdot \mathbf{u} = 0$  for the radial and axial components in cylindrical coordinates, as

$$\frac{1}{r} \frac{\partial(ru_r)}{\partial r} + \frac{\partial u_z}{\partial z} = \frac{1}{r} \frac{\partial}{\partial r} \left( -\frac{\partial \vartheta}{\partial z} \right) + \frac{\partial}{\partial z} \left( \frac{1}{r} \frac{\partial \vartheta}{\partial r} \right) = 0. \quad (6.21)$$

The random numbers are generated independently at each grid point, providing spatially uncorrelated perturbations across all directions. This initialization procedure yields an almost divergence-free velocity field that satisfies all physical boundary conditions while containing the characteristic Taylor vortex structure with realistic boundary layers near the endplates.

### A.2. Angular momentum flux: extension for no-slip boundaries

We now validate the necessity and correctness of the introduced and extended angular momentum flux formulation. Figure 14 compares the radial profiles of  $J^\omega(r)/J_0^\omega$  computed using two different methods. The first approach employs the periodic boundary approximation (figure 14 dotted lines), which neglects axial transport terms. This formulation yields:

$$J_{\text{periodic}}^\omega = r^3 \left( \langle u_r \omega \rangle_{A,t} - \nu \partial_r \langle \omega \rangle_{A,t} \right). \quad (6.22)$$

The second approach uses the no-slip boundary formulation (figure 14 solid lines), which includes the axial correction term  $J_{\text{axial}}$  derived in section 2, accounting for z-dependent angular momentum transport through Ekman layers:

$$J_{\text{total}}^\omega = r^3 \left( \langle u_r \omega \rangle_{A,t} - \nu \partial_r \langle \omega \rangle_{A,t} \right) + \int_{r_1}^r r'^3 \left( \langle \partial_z(u_z \omega) \rangle_{A,t} - \nu \langle \partial_z^2(\omega) \rangle_{A,t} \right) dr'. \quad (6.23)$$

The periodic approximation produces angular momentum flux profiles that vary strongly with radius. This radial dependence is physically inconsistent, since a statistically steady state with no internal sources or sinks demands a conserved and therefore constant angular momentum flux across the gap. In contrast, the extended formulation including axial terms yields constant angular momentum flux profiles across the gap for all Reynolds numbers tested. This behavior is maintained throughout the parameter range  $Re \in [160, 4500]$ , including multiple flow regimes from laminar Taylor vortex flow to turbulent Taylor-vortex flow.

The necessity of the axial correction term  $J_{\text{axial}}$  demonstrates that Ekman layer pumping at the endwalls significantly redistributes angular momentum in the axial direction. Neglecting this redistribution violates conservation and leads to anomalous radial gradients in computed transport quantities. Our results confirm that proper treatment of no-slip boundary conditions requires explicit accounting for three-dimensional momentum transport, beyond what is captured by periodic approximations.

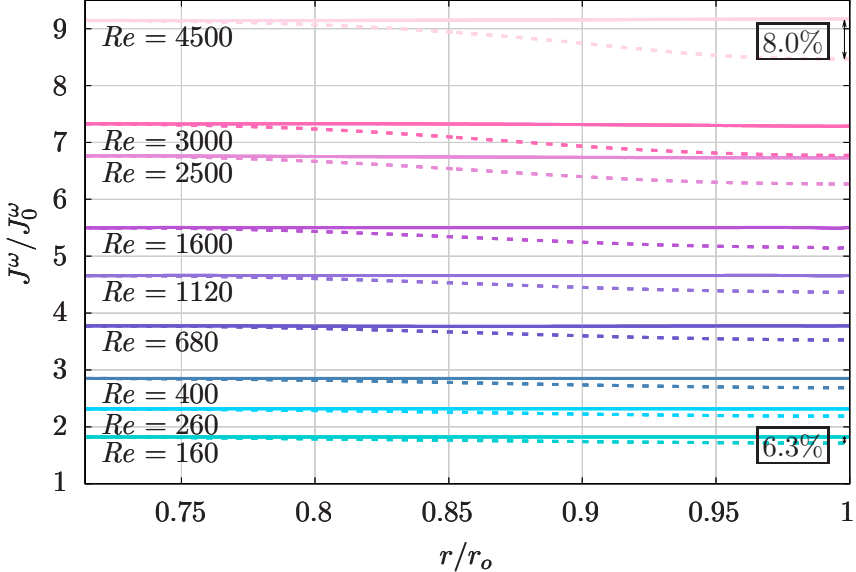


Figure 14. Radial dependence of normalised angular momentum flux for  $160 \leq Re \leq 4.5 \times 10^3$  in the setup of Ostilla *et al.* (2013) for  $\Gamma = 2\pi$  and  $\eta = 5/7$ . Differences between the periodic approximation and the full no-slip consideration approaches are pronounced. Contribution of the “periodic” past, i.e.  $\langle J_r \rangle_{z,t}$  in total  $J^\omega$ , is dominant, but not sufficient for accurate calculation of  $J^\omega$ , which must be constant for all values of  $r$ .

### A.3. Resolution study

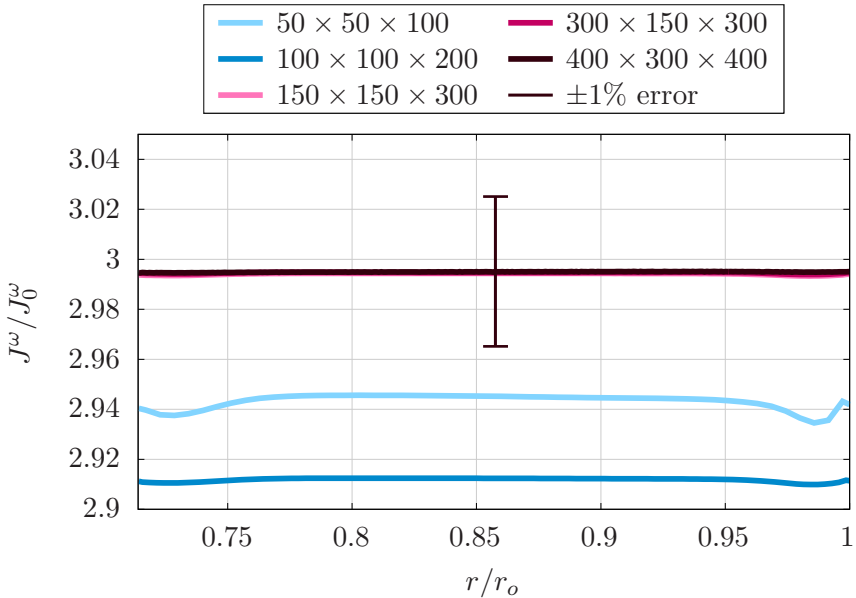


Figure 15. Radial dependence of normalised angular momentum flux for five different grid resolutions ( $N_\phi \times N_r \times N_z$ ). Control parameters were chosen as in Ostilla *et al.* (2013):  $Ta = 2.44 \times 10^5$ ,  $\Gamma = 2\pi$ ,  $\eta = 5/7$ , with no-slip endwall boundary conditions. A 1% error bar is presented, highlighting the sufficiently well resolved cases.

Figure 15 shows results of a grid resolution study for  $Ta = 2.44 \times 10^5$ , corresponding to the setup studied by Ostilla *et al.* (2013), but with no-slip endwalls. The results reveal that the two lowest resolution configurations deliver inaccurate angular momentum flux measurements, which directly highlights the discrepancies that can occur when the smoothing region is insufficiently resolved.

#### A.4. Simulation results

Table 2. Overview of conducted direct numerical simulations. Listed are: Reynolds number  $Re$ , Taylor number  $Ta$ , grid resolution  $N_\phi \times N_r \times N_z$ , initial number of rolls  $n_{\text{initial}}$ , aspect ratio  $\Gamma$ , normalized angular momentum flux  $J^\omega/J_0^\omega$ , total simulation time  $t_{\text{total}}$  in rotational time units, maximum grid spacing to Kolmogorov length ratio  $\max\langle\delta/\eta\rangle$  (averaged over  $\phi, z, t$ ), and corresponding section in text.

$Re$	$Ta$	$N_\phi \times N_r \times N_z$	$n_{\text{initial}}$	$\Gamma$	$J^\omega/J_0^\omega$	$t_{\text{total}}$	$\max\langle\delta/\eta\rangle_{\phi,z,t}$	Section
100	$1.108 \times 10^4$	$256 \times 64 \times 256$	0	30	0.949	900	0.185	4.1
200	$4.431 \times 10^4$	$256 \times 64 \times 256$	0	30	1.615	900	0.268	4.1
300	$9.969 \times 10^4$	$256 \times 64 \times 256$	0	30	2.189	900	0.356	4.1
400	$1.772 \times 10^5$	$256 \times 64 \times 256$	0	30	2.599	900	0.442	4.1
500	$2.769 \times 10^5$	$256 \times 64 \times 256$	0	30	2.952	900	0.531	4.1
600	$3.988 \times 10^5$	$256 \times 64 \times 256$	0	30	3.281	900	0.610	4.1
90	$8.916 \times 10^3$	$256 \times 64 \times 128$	0	11	1.034	200	0.433	4.3
95	$9.934 \times 10^3$	$256 \times 64 \times 128$	0	11	1.036	200	0.446	4.3
101	$1.123 \times 10^4$	$256 \times 64 \times 128$	0	11	1.037	200	0.459	4.3
105	$1.214 \times 10^4$	$256 \times 64 \times 128$	0	11	1.039	200	0.468	4.3
110	$1.332 \times 10^4$	$256 \times 64 \times 128$	0	11	1.041	200	0.477	4.3
115	$1.456 \times 10^4$	$256 \times 64 \times 128$	0	11	1.044	200	0.487	4.3
120	$1.585 \times 10^4$	$256 \times 64 \times 128$	0	11	1.046	200	0.497	4.3
125	$1.712 \times 10^4$	$256 \times 64 \times 128$	0	11	1.051	200	0.508	4.3
131	$1.889 \times 10^4$	$256 \times 64 \times 128$	0	11	1.058	200	0.519	4.3
135	$2.006 \times 10^4$	$256 \times 64 \times 128$	0	11	1.066	200	0.528	4.3
140	$2.157 \times 10^4$	$256 \times 64 \times 128$	0	11	1.081	200	0.538	4.3
145	$2.314 \times 10^4$	$256 \times 64 \times 128$	0	11	1.137	200	0.556	4.3
151	$2.510 \times 10^4$	$256 \times 64 \times 128$	0	11	1.208	200	0.576	4.3
155	$2.645 \times 10^4$	$256 \times 64 \times 128$	0	11	1.257	200	0.591	4.3
160	$2.818 \times 10^4$	$256 \times 64 \times 128$	0	11	1.307	200	0.606	4.3
165	$2.997 \times 10^4$	$256 \times 64 \times 128$	0	11	1.365	200	0.626	4.3
172	$3.256 \times 10^4$	$256 \times 64 \times 128$	0	11	1.431	200	0.651	4.3
180	$3.556 \times 10^4$	$256 \times 64 \times 128$	0	11	1.503	200	0.675	4.3
190	$3.974 \times 10^4$	$256 \times 64 \times 128$	0	11	1.596	200	0.707	4.3
200	$4.403 \times 10^4$	$256 \times 64 \times 128$	0	11	1.680	200	0.738	4.3
210	$4.854 \times 10^4$	$256 \times 64 \times 128$	0	11	1.758	200	0.768	4.3
220	$5.328 \times 10^4$	$256 \times 64 \times 128$	0	11	1.829	200	0.796	4.3
230	$5.823 \times 10^4$	$256 \times 64 \times 128$	0	11	1.896	200	0.824	4.3
1500	$2.492 \times 10^6$	$1536 \times 128 \times 768$	0	30	5.196	500	0.302	4.3
2000	$4.431 \times 10^6$	$1536 \times 128 \times 768$	0	30	5.783	500	0.364	4.3
2500	$6.923 \times 10^6$	$1536 \times 128 \times 768$	0	30	6.424	500	0.436	4.3
3000	$9.969 \times 10^6$	$1536 \times 128 \times 768$	0	30	7.036	500	0.508	4.3
3500	$1.357 \times 10^7$	$1536 \times 128 \times 768$	0	30	7.522	500	0.574	4.3
4000	$1.772 \times 10^7$	$1536 \times 128 \times 768$	0	30	7.487	500	0.652	4.3
4500	$2.243 \times 10^7$	$1792 \times 256 \times 1024$	0	30	7.960	500	0.721	4.3
5000	$2.769 \times 10^7$	$1792 \times 256 \times 1024$	0	30	8.262	500	0.782	4.3
5500	$3.351 \times 10^7$	$1792 \times 256 \times 1024$	0	30	8.446	500	0.841	4.3
6000	$3.988 \times 10^7$	$1792 \times 256 \times 1024$	0	30	8.935	500	0.896	4.3
6500	$4.680 \times 10^7$	$1792 \times 256 \times 1024$	0	30	9.205	500	0.964	4.3

Continued on next page

Re	Ta	$N_\phi \times N_r \times N_z$	$n_{\text{initial}}$	$\Gamma$	$J^\omega / J_0^\omega$	$t_{\text{total}}$	$\max \langle \delta / \eta \rangle_{\phi, z, t}$	Section
7000	$5.427 \times 10^7$	$1792 \times 256 \times 1024$	0	30	9.845	500	1.026	4.3
7500	$6.230 \times 10^7$	$1792 \times 256 \times 1024$	0	30	10.233	500	1.087	4.3
400	$1.772 \times 10^5$	$256 \times 64 \times 256$	18	30	2.099	650	0.467	4.3
400	$1.772 \times 10^5$	$256 \times 64 \times 256$	20	30	2.148	650	0.473	4.3
400	$1.772 \times 10^5$	$256 \times 64 \times 256$	22	30	2.274	650	0.481	4.3
400	$1.772 \times 10^5$	$256 \times 64 \times 256$	24	30	2.307	650	0.487	4.3
400	$1.772 \times 10^5$	$256 \times 64 \times 256$	26	30	2.331	650	0.490	4.3
400	$1.772 \times 10^5$	$256 \times 64 \times 256$	28	30	2.392	650	0.496	4.3
500	$2.769 \times 10^5$	$256 \times 64 \times 256$	18	30	2.367	820	0.547	4.3
500	$2.769 \times 10^5$	$256 \times 64 \times 256$	20	30	2.422	820	0.557	4.3
500	$2.769 \times 10^5$	$256 \times 64 \times 256$	22	30	2.567	820	0.568	4.3
500	$2.769 \times 10^5$	$256 \times 64 \times 256$	24	30	2.611	820	0.576	4.3
500	$2.769 \times 10^5$	$256 \times 64 \times 256$	26	30	2.648	820	0.582	4.3
500	$2.769 \times 10^5$	$256 \times 64 \times 256$	28	30	2.726	820	0.595	4.3
600	$3.988 \times 10^5$	$256 \times 64 \times 256$	18	30	2.617	920	0.631	4.3
600	$3.988 \times 10^5$	$256 \times 64 \times 256$	20	30	2.690	920	0.646	4.3
600	$3.988 \times 10^5$	$256 \times 64 \times 256$	22	30	2.839	920	0.657	4.3
600	$3.988 \times 10^5$	$256 \times 64 \times 256$	24	30	2.899	920	0.668	4.3
600	$3.988 \times 10^5$	$256 \times 64 \times 256$	26	30	2.946	920	0.677	4.3
600	$3.988 \times 10^5$	$256 \times 64 \times 256$	28	30	3.029	920	0.693	4.3
700	$5.427 \times 10^5$	$256 \times 64 \times 256$	18	30	2.837	1050	0.713	4.3
700	$5.427 \times 10^5$	$256 \times 64 \times 256$	20	30	2.932	1050	0.728	4.3
700	$5.427 \times 10^5$	$256 \times 64 \times 256$	22	30	3.084	1050	0.748	4.3
700	$5.427 \times 10^5$	$256 \times 64 \times 256$	24	30	3.170	1050	0.760	4.3
700	$5.427 \times 10^5$	$256 \times 64 \times 256$	26	30	3.218	1050	0.771	4.3
700	$5.427 \times 10^5$	$256 \times 64 \times 256$	28	30	3.312	1050	0.784	4.3
800	$7.089 \times 10^5$	$256 \times 64 \times 256$	18	30	3.045	1200	0.796	4.3
800	$7.089 \times 10^5$	$256 \times 64 \times 256$	20	30	3.139	1200	0.808	4.3
800	$7.089 \times 10^5$	$256 \times 64 \times 256$	22	30	3.307	1200	0.837	4.3
800	$7.089 \times 10^5$	$256 \times 64 \times 256$	24	30	3.411	1200	0.848	4.3
800	$7.089 \times 10^5$	$256 \times 64 \times 256$	26	30	3.477	1200	0.861	4.3
800	$7.089 \times 10^5$	$256 \times 64 \times 256$	28	30	3.533	1200	0.868	4.3
900	$8.972 \times 10^5$	$256 \times 64 \times 256$	18	30	3.240	1300	0.878	4.3
900	$8.972 \times 10^5$	$256 \times 64 \times 256$	20	30	3.340	1300	0.891	4.3
900	$8.972 \times 10^5$	$256 \times 64 \times 256$	22	30	3.473	1300	0.905	4.3
900	$8.972 \times 10^5$	$256 \times 64 \times 256$	24	30	3.445	1300	0.908	4.3
900	$8.972 \times 10^5$	$256 \times 64 \times 256$	26	30	3.458	1300	0.913	4.3
900	$8.972 \times 10^5$	$256 \times 64 \times 256$	28	30	3.447	1300	0.911	4.3
1000	$1.108 \times 10^6$	$768 \times 256 \times 384$	18	30	3.426	860	0.957	4.3
1000	$1.108 \times 10^6$	$768 \times 256 \times 384$	20	30	3.578	860	0.973	4.3
1000	$1.108 \times 10^6$	$768 \times 256 \times 384$	22	30	3.644	860	0.991	4.3
1000	$1.108 \times 10^6$	$768 \times 256 \times 384$	24	30	3.519	860	0.974	4.3
1000	$1.108 \times 10^6$	$768 \times 256 \times 384$	26	30	3.648	860	0.990	4.3
1000	$1.108 \times 10^6$	$768 \times 256 \times 384$	28	30	3.573	860	0.983	4.3
1250	$1.731 \times 10^6$	$768 \times 256 \times 384$	18	30	3.769	1020	1.142	4.3
1250	$1.731 \times 10^6$	$768 \times 256 \times 384$	20	30	3.875	1020	1.178	4.3
1250	$1.731 \times 10^6$	$768 \times 256 \times 384$	22	30	3.887	1020	1.176	4.3
1250	$1.731 \times 10^6$	$768 \times 256 \times 384$	24	30	3.875	1020	1.184	4.3
1250	$1.731 \times 10^6$	$768 \times 256 \times 384$	26	30	3.891	1020	1.190	4.3
1250	$1.731 \times 10^6$	$768 \times 256 \times 384$	28	30	3.902	1020	1.185	4.3
1500	$2.492 \times 10^6$	$768 \times 256 \times 384$	18	30	4.100	830	1.333	4.3
1500	$2.492 \times 10^6$	$768 \times 256 \times 384$	20	30	4.105	830	1.341	4.3
1500	$2.492 \times 10^6$	$768 \times 256 \times 384$	22	30	4.108	830	1.353	4.3
1500	$2.492 \times 10^6$	$768 \times 256 \times 384$	24	30	4.228	830	1.356	4.3

Continued on next page

Re	Ta	$N_\phi \times N_r \times N_z$	$n_{\text{initial}}$	$\Gamma$	$J^\omega/J_0^\omega$	$t_{\text{total}}$	$\max \langle \delta/\eta \rangle_{\phi,z,t}$	Section
1500	$2.492 \times 10^6$	$768 \times 256 \times 384$	26	30	4.214	830	1.364	4.3
1500	$2.492 \times 10^6$	$768 \times 256 \times 384$	28	30	4.120	830	1.348	4.3
2000	$4.431 \times 10^6$	$1536 \times 128 \times 768$	18	30	4.750	400	0.350	4.3
2000	$4.431 \times 10^6$	$1536 \times 128 \times 768$	20	30	4.977	400	0.356	4.3
2000	$4.431 \times 10^6$	$1536 \times 128 \times 768$	22	30	5.076	400	0.359	4.3
2000	$4.431 \times 10^6$	$1536 \times 128 \times 768$	24	30	5.199	400	0.359	4.3
2000	$4.431 \times 10^6$	$1536 \times 128 \times 768$	26	30	5.199	400	0.362	4.3
2000	$4.431 \times 10^6$	$1536 \times 128 \times 768$	28	30	5.438	400	0.382	4.3
3000	$9.969 \times 10^6$	$1536 \times 128 \times 768$	18	30	5.718	300	0.483	4.3
3000	$9.969 \times 10^6$	$1536 \times 128 \times 768$	20	30	5.934	300	0.490	4.3
3000	$9.969 \times 10^6$	$1536 \times 128 \times 768$	22	30	6.142	300	0.496	4.3
3000	$9.969 \times 10^6$	$1536 \times 128 \times 768$	24	30	6.331	300	0.509	4.3
3000	$9.969 \times 10^6$	$1536 \times 128 \times 768$	26	30	6.529	300	0.511	4.3
3000	$9.969 \times 10^6$	$1536 \times 128 \times 768$	28	30	6.525	300	0.518	4.3
$400.9 \times 10^3$	$2.440 \times 10^5$	$100 \times 50 \times 50$	0	$2\pi$	2.942	1688	3.191	A.3
$400.9 \times 10^3$	$2.440 \times 10^5$	$200 \times 100 \times 100$	0	$2\pi$	2.911	252	1.557	A.3
$400.9 \times 10^3$	$2.440 \times 10^5$	$300 \times 150 \times 150$	0	$2\pi$	2.994	744	1.089	A.3
$400.9 \times 10^3$	$2.440 \times 10^5$	$300 \times 150 \times 300$	0	$2\pi$	2.995	790	0.447	A.3
$400.9 \times 10^3$	$2.440 \times 10^5$	$400 \times 300 \times 400$	0	$2\pi$	2.995	306	0.438	A.3

## REFERENCES

AHLERS, G., GROSSMANN, S. & LOHSE, D. 2009 Heat transfer and large scale dynamics in turbulent Rayleigh–Bénard convection. *Rev. Mod. Phys.* **81** (2), 503–537.

BATTEN, W. M. J., BRESSLOFF, N. W. & TURNOCK, S. R. 2002 Numerical simulations of the evolution of Taylor cells from a growing boundary layer on the inner cylinder of a high radius ratio Taylor–Couette system. *Phys. Rev. E* **66** (6), 066302.

BILSON, M. & BREMHRST, K. 2007 Direct numerical simulation of turbulent Taylor–Couette flow. *J. Fluid Mech.* **579**, 227–270.

BRAUCKMANN, H. J. & ECKHARDT, B. 2013 Direct numerical simulations of local and global torque in Taylor–Couette flow up to  $Re = 30\,000$ . *J. Fluid Mech.* **718**, 398–427.

COLES, D. 1965 Transition in circular Couette flow. *J. Fluid Mech.* **21** (3), 385–425.

COUGHLIN, K. & MARCUS, P. S. 1996 Turbulent bursts in Couette–Taylor flow. *Phys. Rev. Lett.* **77** (11), 2214–2217.

CZARNY, O., SERRE, E., BONTOUX, P. & LUEPTOW, R. M. 2004 Interaction of wavy cylindrical Couette flow with endwalls. *Phys. Fluids* **16** (4), 1140–1148.

DI PRIMA, R. C. & SWINNEY, H. L. 1981 Instabilities and transition in flow between concentric rotating cylinders. In *Hydrodynamic Instabilities and the Transition to Turbulence* (ed. H. L. Swinney & J. P. Gollub), pp. 139–180. Berlin: Springer-Verlag.

DUTCHER, C. S. & MULLER, S. J. 2009 Spatio-temporal mode dynamics and higher order transitions in high aspect ratio Newtonian Taylor–Couette flows. *J. Fluid Mech.* **641**, 85–113.

ECKE, R. E., ZHANG, X. & SHISHKINA, O. 2022 Connecting wall modes and boundary zonal flows in rotating Rayleigh–Bénard convection. *Phys. Rev. Fluids* **7** (1), L011501.

ECKHARDT, B., GROSSMANN, S. & LOHSE, D. 2007 Torque scaling in turbulent Taylor–Couette flow between independently rotating cylinders. *J. Fluid Mech.* **581**, 221–250.

EMRAN, M. S. & SHISHKINA, O. 2020 Natural convection in cylindrical containers with isothermal ring-shaped obstacles. *J. Fluid Mech.* **882**, A3.

FENSTERMACHER, P. R., SWINNEY, H. L. & GOLLUB, J. P. 1979 Dynamical instabilities and the transition to chaotic Taylor vortex flow. *J. Fluid Mech.* **94** (1), 103–128.

FROITZHEIM, A. 2019 Angular momentum transport and flow organization in Taylor–Couette flow at radius ratio of  $\eta = 0.357$ . *Phys. Rev. Fluids* **4** (8), 084605.

VAN GILS, D. P. M., HUISMAN, S. G., BRUGGERT, G.-W., SUN, C. & LOHSE, D. 2011 Torque scaling in turbulent Taylor–Couette flow with co- and counterrotating cylinders. *Phys. Rev. Lett.* **106** (2), 024502.

HORN, S. & SCHMID, P. J. 2017 Prograde, retrograde, and oscillatory modes in rotating Rayleigh–Bénard convection. *J. Fluid Mech.* **831**, 182–211.

HORN, S. & SHISHKINA, O. 2015 Toroidal and poloidal energy in rotating Rayleigh–Bénard convection. *J. Fluid Mech.* **762**, 232–255.

HUISMAN, S. G., VAN DER VEEN, R. C. A., SUN, C. & LOHSE, D. 2014 Multiple states in highly turbulent Taylor–Couette flow. *Nat. Commun.* **5**, 3820.

JEGANATHAN, V., ALBA, K. & OSTILLA-MÓNICO, R. 2021 Controlling secondary flows in Taylor–Couette flow using stress-free boundary conditions. *J. Fluid Mech.* **922**, A17.

LENG, X.-Y. & ZHONG, J.-Q. 2022 Aspect-ratio dependence of heat and angular momentum transport in turbulent Taylor–Couette flows with axial thermal forcing. *Int. J. Heat Mass Transf.* **195**, 123194.

MAMUN, C. K. & TUCKERMAN, L. S. 1995 Asymmetry and Hopf bifurcation in spherical Couette flow. *Phys. Fluids* **7** (1), 80–91.

MARTÍNEZ-ARIAS, B., PEIXINHO, J., CRUMEYROLLE, O. & MUTABAZI, I. 2014 Effect of the number of vortices on the torque scaling in Taylor–Couette flow. *J. Fluid Mech.* **748**, 756–767.

MCCORMACK, M., TEIMURAZOV, A., SHISHKINA, O. & LINKMANN, M. 2025 Subcritical transition and multistability in liquid-metal magnetoconvection with sidewalls. *J. Fluid Mech.* **1023**, R1.

OSTILLA, R., STEVENS, R. J. A. M., GROSSMANN, S., VERZICCO, R. & LOHSE, D. 2013 Optimal Taylor–Couette flow: direct numerical simulations. *J. Fluid Mech.* **719**, 14–46.

OSTILLA-MÓNICO, R., VAN DER POEL, E. P., VERZICCO, R., GROSSMANN, S. & LOHSE, D. 2014 Exploring the phase diagram of fully turbulent Taylor–Couette flow. *J. Fluid Mech.* **761**, 1–26.

PIRRÒ, D. & QUADRID, M. 2008 Direct numerical simulation of turbulent Taylor–Couette flow. *Eur. J. Mech. B Fluids* **27** (5), 552–566.

VAN DER POEL, E. P., STEVENS, R. J. A. M. & LOHSE, D. 2011 Connecting flow structures and heat flux in turbulent Rayleigh–Bénard convection. *Phys. Rev. E* **84** (4), 045303.

PONCET, S., DA SOGHE, R., BIANCHINI, C., VIAZZO, S. & AUBERT, A. 2013 Turbulent Couette–Taylor flows with endwall effects: a numerical benchmark. *Int. J. Heat Fluid Flow* **44**, 229–238.

POPE, S. B. 2000 *Turbulent flows*. Cambridge University Press.

RAMESH, P., BHARADWAJ, S. & ALAM, M. 2019 Suspension Taylor–Couette flow: co-existence of stationary and travelling waves, and the characteristics of Taylor vortices and spirals. *J. Fluid Mech.* **870**, 901–940.

REITER, P., ZHANG, X. & SHISHKINA, O. 2022 Flow states and heat transport in Rayleigh–Bénard convection with different sidewall boundary conditions. *J. Fluid Mech.* **936**, A32.

REITER, P., ZHANG, X., STEPANOV, R. & SHISHKINA, O. 2021 Generation of zonal flows in convective systems by travelling thermal waves. *J. Fluid Mech.* **913**, A13.

RUDELSTORFER, G., GREIL, R., VOGI, M., SIEBENHOFER, M., LUX, S. & GRAFSCHAFTER, A. 2023 Gas/liquid operations in the Taylor–Couette disc contactor: continuous chemisorption of CO<sub>2</sub>. *Processes* **11** (6), 1614.

RUELLE, D. & TAKENS, F. 1971 On the nature of turbulence. *Commun. Math. Phys.* **20** (3), 167–192.

SCHRIMPF, M., ESTEBAN, J., WARMELING, H., FÄRBER, T., BEHR, A. & VORHOLT, A. J. 2021 Taylor–Couette reactor: principles, design, and applications. *AIChE J.* **67** (5), e17228.

SHISHKINA, O., HORN, S., WAGNER, S. & CHING, E. S. C. 2015 Thermal boundary layer equation for turbulent Rayleigh–Bénard convection. *Phys. Rev. Lett.* **114** (11), 114302.

TAYLOR, G. I. 1923 Stability of a viscous liquid contained between two rotating cylinders. *Proc. R. Soc. Lond. A* **102** (718), 541–542.

WANG, Q., VERZICCO, R., LOHSE, D. & SHISHKINA, O. 2020 Multiple states in turbulent large-aspect-ratio thermal convection: what determines the number of convection rolls? *Phys. Rev. Lett.* **125** (7), 074501.

WANG, Q., WAN, Z.-H., YAN, R. & SUN, D.-J. 2018 Multiple states and heat transfer in two-dimensional tilted convection with large aspect ratios. *Phys. Rev. Fluids* **3** (11), 113503.

WENDT, F. 1933 Turbulente Strömungen zwischen zwei rotierenden konaxialen Zylindern. *Ing.-Arch.* **4** (6), 577–595.

XU, F., SU, J., LAN, B., ZHAO, P., HE, Y., SUN, C. & WANG, J. 2023 Direct numerical simulation of Taylor–Couette flow with vertical asymmetric rough walls. *J. Fluid Mech.* **975**, A30.

YANG, Y., CHEN, W., VERZICCO, R. & LOHSE, D. 2020 Multiple states and transport properties of double-diffusive convection turbulence. *Proc. Natl. Acad. Sci. USA* **117** (26), 14676–14681.

YAO, Z., EMRAN, M. S., TEIMURAZOV, A. & SHISHKINA, O. 2025 Direct numerical simulations of centrifugal convection: from gravitational to centrifugal buoyancy dominance. *Int. J. Heat Mass Transf.* **236**, 126314.

ZHANG, X., ECKE, R. E. & SHISHKINA, O. 2021 Boundary zonal flows in rapidly rotating turbulent thermal convection. *J. Fluid Mech.* **915**, A62.

ZHANG, X., VAN GILS, D. P. M., HORN, S., WEDI, M., ZWIRNER, L., AHLERS, G., ECKE, R. E., WEISS, S., BODENSCHATZ, E. & SHISHKINA, O. 2020 Boundary zonal flow in rotating turbulent Rayleigh–Bénard convection. *Phys. Rev. Lett.* **124** (8), 084505.

ZHANG, X., REITER, P., SHISHKINA, O. & ECKE, R. E. 2024 Wall modes and the transition to bulk convection in rotating Rayleigh–Bénard convection. *Phys. Rev. Fluids* **9** (5), 053501.